



SRON-AHEAD-RP-2018-001

Developed H/W components: X-ray microcalorimeter detector

Version 1.0

Date : 6 September 2018

Written by	XIFU SRON & CSIC Teams
Approved by	
Distribution List	Lourdes Fabrega Gao Jian-Rong Pourya Khosropanah Lorenzo Natalucci AHEAD Management Team H2020 Participant Portal
Distribution Date	06/09/2018



SRON-AHEAD-RP-2018-001

This activity is a combined effort from SRON/Netherlands and CSIC/Spain and is reported in three different documents which are concatenated for this report:

- Report Mo/Au TES fabrication (CSIC-AHEAD-WP6.2b-fab)
- Report Mo/Au TES test (CSIC AHEAD report WP 6.2b-test)
- TiAu pixel design update (SRON-XIFU-TN-2015-063)

	WP6 Detectors	Doc. no. : CSIC AHEAD Report WP6.2b-fab Issue : draft 1.0 Date : 14/5/2018 Page : 1 of 18
	WP6.2. X-ray sensors <i>WP6.2b Mo/Au pixels</i>	

Title: Report WP6.2b, Mo/Au TES fabrication

Prepared by : Lourdes Fàbrega, Agustín Camón, Pavel Strichovanec, Javier Moral-Vico, Nieves Casañ-Pastor

	<p>WP6 Detectors</p> <p>WP6.2. X-ray sensors</p> <p><i>WP6.2b Mo/Au pixels</i></p>	<p>Doc. no.: CSIC AHEAD Report WP6.2b-fab</p> <p>Issue : draft 1.0</p> <p>Date : 14/5/2018</p> <p>Page : 2 of 18</p>
		

Contents

ABBREVIATIONS AND ACRONYMS	3
APPLICABLE DOCUMENTS	3
REFERENCE DOCUMENTS	3
1. SUMMARY	4
2. Mo/Au microcalorimeters	4
2.1. Mo/Au bilayers	4
2.2. TES Designs	6
2.3. TES fabrication	8
2.3.1. Bilayer deposition	8
2.3.2. TES fabrication procedure	9
3. X-ray absorbers	12
3.1 Electrodeposition of Bi and Au	12
3.2 Absorber design	15
3.3 Absorber fabrication procedure	16
4. CONCLUSIONS	18
5. FUTURE WORK	18

	<p>WP6 Detectors</p> <p>WP6.2. X-ray sensors</p>	<p>Doc. no.: CSIC AHEAD Report WP6.2b-fab</p> <p>Issue : draft 1.0</p> <p>Date : 14/5/2018</p> <p>Page : 3 of 18</p>
	<p><i>WP6.2b Mo/Au pixels</i></p>	

ABBREVIATIONS AND ACRONYMS

Item	Meaning
------	---------

FIB	Focused Ion Beam
IM	Ion Milling
RIE	Reactive Ion Etching
RRR	Residual Resistance Ratio
SEM	Scanning Electron Microscopy
TES	Transition Edge Sensor
UHV	Ultra High Vacuum
WP	Work Package
XPS	X-ray Photoemission Spectroscopy
XRD	X-ray Diffraction
XRR	X-ray Reflectometry

APPLICABLE DOCUMENTS

[AD#]	Document reference	Title
-------	--------------------	-------

[AD1]	CSIC AHEAD Report WP6.2b-test 1.0	Mo/Au pixel test
-------	-----------------------------------	------------------

REFERENCE DOCUMENTS

[RD#]	Reference
-------	-----------

[RD1]	L.Fàbrega et al., "Effects of stress and morphology on the resistivity and critical temperature of room temperature sputtered Mo thin films", IEEE, Trans. Appl. Supercond. 19, 3779 (2009)
[RD2]	L. Fàbrega et al., "Mo-based proximity bilayers for TES: microstructure and properties", IEEE Trans. Appl. Supercond. 19, 460 (2009)
[RD3]	L. Fàbrega et al., "Size and dimensionality effects in superconducting Mo thin films", Supercond. Sci. Technol. 24, 075014 (2011)
[RD4]	J.M.Martinis et al., "Calculation of T _c in a normal-superconductor bilayer using microscopic-based Usadel Theory", Nucl. Instrum. Meth. Phys. A 444, 23 (2000)
[RD5]	M.Parra-Borderías et al., "Thermal stability of Mo/Au bilayers for TES applications", Supercond. Sci. Technol. 25, 095001 (2012)
[RD6]	G.C.Hilton et al., "Microfabricated Transition-Edge X-ray Detectors", IEEE Trans. Appl. Supercond. 11, pp. 739 (2001)
[RD7]	J.Moral-Vico et al., "Microstructure and electrical transport in electrodeposited Bi films", submitted to J. Electroanalytical Chem.

	<p>WP6 Detectors</p> <p>WP6.2. X-ray sensors</p> <p><i>WP6.2b Mo/Au pixels</i></p>	<p>Doc. no.: CSIC AHEAD Report WP6.2b-fab</p> <p>Issue : draft 1.0</p> <p>Date : 14/5/2018</p> <p>Page : 4 of 18</p>
		

1. SUMMARY

This document describes the design and fabrication of Mo/Au TES pixels carried out by CSIC within Work Package 6.2b (WP6.2b). It is divided in two main parts, describing respectively the design and fabrication procedures of Mo/Au microcalorimeters (section 2) and absorbers (section 3). It includes the description of the bilayers used, the TES designs, the TES fabrication procedure and its evolution during the period of work within this project, and the characteristics and fabrication procedures of electrodeposited absorbers. The document ends with conclusions (section 4) and lines of projected future work (section 5).

2. Mo/Au microcalorimeters

This section describes the design and fabrication procedure of the microcalorimeters (without absorber). First (section 2.1) details of the Mo/Au bilayers and thicknesses choice are provided. Next (section 2.2) the designs are described. Finally (section 2.3) the fabrication procedure and its optimization are given.

2.1. Mo/Au bilayers

Molybdenum is a material that oxidizes very easily and which displays superconductivity strongly affected by impurities and stress [RD1]. Therefore, thin film deposition in a UHV chamber is required in order to achieve acceptable T_c reproducibility; we use RF magnetron sputtering [RD1]. The deposition systems are described in detail in section 2.3.

Material	thickness	ρ_{res} (n Ω m)
Mo, sputtered	50nm	125
Au, sputtered	15nm	39
Au, e-beam	15nm	16
Au, e-beam	>100nm	4

Table 1. Resistivity values of the Mo and Au films that constitute the TES, for the used thicknesses.

The resistance of Mo/Au bilayers with T_c in the range of 100 mK is dominated by the resistivity of the Au layer. Because of the larger grain size, Au films deposited by e-beam display lower resistivity than sputtered Au films (see Table 1), being therefore more suitable to obtain TES with low R_n . Due to the impossibility of depositing Au by e-beam in the UHV chamber used to deposit Mo, and in order to prevent contamination of the Mo surface and therefore degradation of the proximity effect, we adopted the so-called "trilayer design" [RD2]: we use a protective 15nm-thick Au layer sputtered in situ after Mo growth, and afterwards another Au layer is deposited ex-situ by e-beam, up to the required total Au thickness d_{Au} .

A good control of thicknesses of each layer is essential, since thickness variations will result in irreproducibility of the bilayers T_c . The thickness of sputtered Mo and Au films is measured by X-ray reflectometry (XRR); for the thicker Au films deposited by e-beam, a profilometer is used. Periodically the growth rates are checked through the deposition of calibrating layers and bilayers. These growth rates are used to determine the deposition times for samples to be fabricated, whose thicknesses are afterwards verified. Usually the thickness control of sputtered Mo and Au is better than 3%, while that of Au by e-beam is of the order of 2-3%, for typical thicknesses required for our TESs.

	<p>WP6 Detectors</p> <p>WP6.2. X-ray sensors</p> <p><i>WP6.2b Mo/Au pixels</i></p>	<p>Doc. no.: CSIC AHEAD Report WP6.2b-fab</p> <p>Issue : draft 1.0</p> <p>Date : 14/5/2018</p> <p>Page : 5 of 18</p>
		

Figs.1a and 1b display calibration curves of Mo/Au bilayers T_c for different d_{Au} and d_{Mo} . In a former study we showed that molybdenum displays finite size effects for thicknesses below ~ 30 nm [RD3]. Hence we settled a Mo thickness to stay safely above this limit, and at the same time access a suitable range of R_n , without using too thick layers that would imply too large heat capacities and too low R_n values; we chose $d_{Mo}=55$ nm. All the TES fabricated and characterized in this project are made of bilayers with 55nm Mo and 335 nm Au, which provide $T_c \sim 100$ mK.

More recently, and in order to produce TESs with higher resistances, we have explored the evolution of T_c for bilayers with d_{Mo} down to 40 nm. This is illustrated on Fig.1c, which evidences that we can produce TES with $T_c=100$ mK for several bilayer thicknesses, between 42/220 and 55/335.

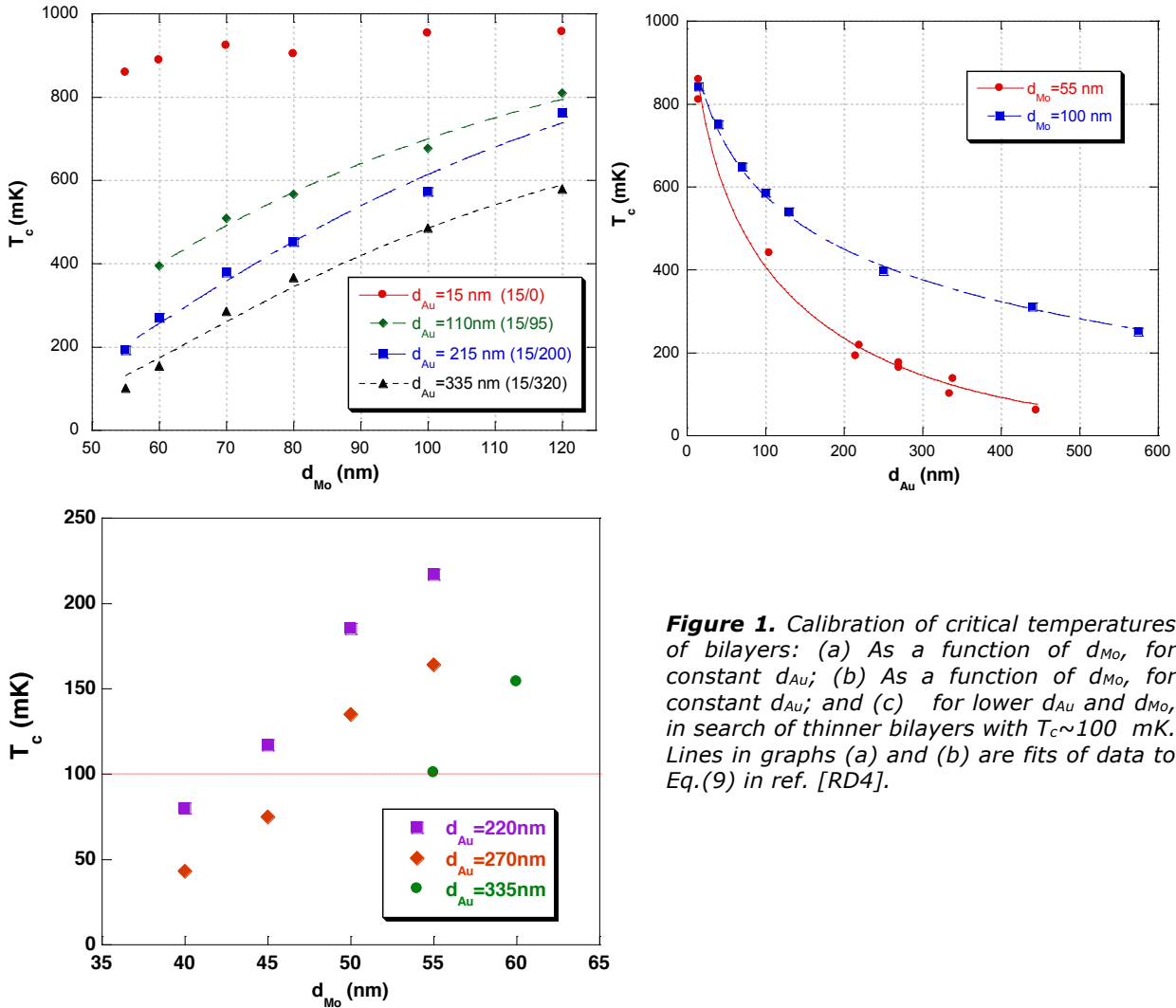


Figure 1. Calibration of critical temperatures of bilayers: (a) As a function of d_{Mo} , for constant d_{Au} ; (b) As a function of d_{Mo} , for constant d_{Au} ; and (c) for lower d_{Au} and d_{Mo} , in search of thinner bilayers with $T_c \sim 100$ mK. Lines in graphs (a) and (b) are fits of data to Eq.(9) in ref. [RD4].

	WP6 Detectors WP6.2. X-ray sensors <i>WP6.2b Mo/Au pixels</i>	Doc. no.: CSIC AHEAD Report WP6.2b-fab Issue : draft 1.0 Date : 14/5/2018 Page : 6 of 18
		

It is to be noted that these bilayers were formerly shown to be stable upon heating up to 150°C [RD5], which makes them good candidates for space applications.

2.2. TES designs

Table 2 describes the wafers and chips used for all the fabricated devices. Two designs have been defined and fabricated; the basic parameters of both of them are included on Table 3.

Wafer	<100> Si
Wafer thickness	500+/-25 μ m
Wafer coatings	Native oxide / low stress Si ₃ N ₄ with $\rho \sim 1-30\Omega\text{cm}$ (both sides)
Si ₃ N ₄ thickness	0.5 or 1 μ m
Chip size	10x10mm ²

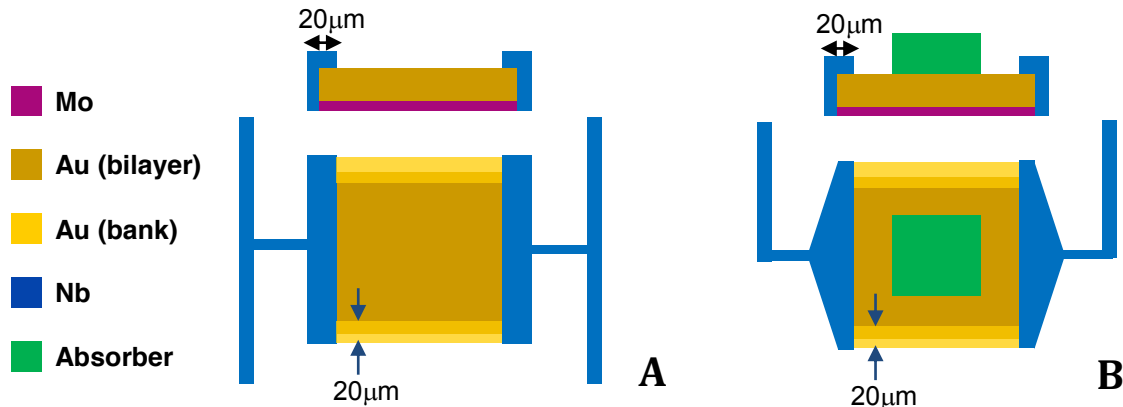
Table 2. Parameters of wafers and chips.

	Design A	Design B
Mo/Au thickness	55nm/335nm	55nm/335nm
Critical temperature	100mK	100mK
Wiring	Nb	Nb or Mo/Nb
Contact pad	Nb	Nb
Membrane area	0.5x0.5 mm ² 1x1 mm ²	0.25x0.25 mm ² 0.5x0.5 mm ² 1x1 mm ²
Membrane thickness	0.5 or 1 μ m	0.5 or 1 μ m
Banks	Yes/No	No
Absorber	No or Bi central (square or mushroom)	No or central mushroom (Bi, Au, Bi/Au)

Table 3. Parameters of the fabricated TES.

Design A

This design, shown on Fig. 2 *left*, was the original design during the definition of the fabrication of the first devices. Individual chips of size 10x10 mm² with membrane opened previously were processed, with the parameters described in Table 3. The Mo/Au squares ranged between 100 and 200 μ m; pads and wiring were made of 150 nm-thick Nb, with $T_c \sim 8.8$ K and $I_c > 20$ mA at 4.2 K. Most devices with this design included banks, i.e. Au strips deposited on the uncovered edges of the bilayer, in order to prevent transition broadening due to T_c inhomogeneities there [RD6]. Progress in fabrication during last year (described in section 2.3.3.) allowed production of TES without banks and excellent transitions, as shown on Fig. 3.



Figures 2. Basic TES designs A and B, as discussed in the text. Both designs can include Au banks, which are eventually added using one more lithography step and mask layer. Nb wiring is used in A, while Nb or Nb/Mo wiring with nearly identical T_c is used in B.

	<p>WP6 Detectors</p> <p>WP6.2. X-ray sensors</p> <p>WP6.2b Mo/Au pixels</p>	<p>Doc. no.: CSIC AHEAD Report WP6.2b-fab</p> <p>Issue : draft 1.0</p> <p>Date : 14/5/2018</p> <p>Page : 7 of 18</p>
		

Design B

Fig.2 *right* displays the evolved design of TESs in the next set of masks, designed to process full 4" wafers. In these masks the chip size was kept to 10x10 mm², but every chip included 3 TES with identical Mo/Au geometry and parameters, each one on a membrane of different size (see Fig. 4): 0.25x0.25 mm² (baseline TES, labelled A), 0.5x0.5 mm² (labelled C) and 1x1 mm² (labelled B); the mask for banks was fabricated but not used, in view of the results with previous design and improved fabrication.

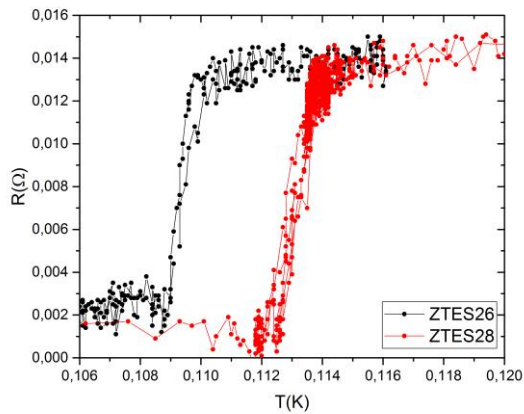
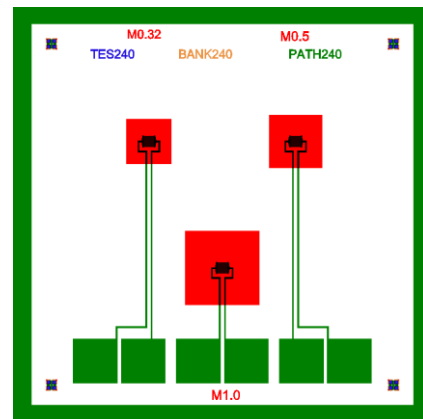
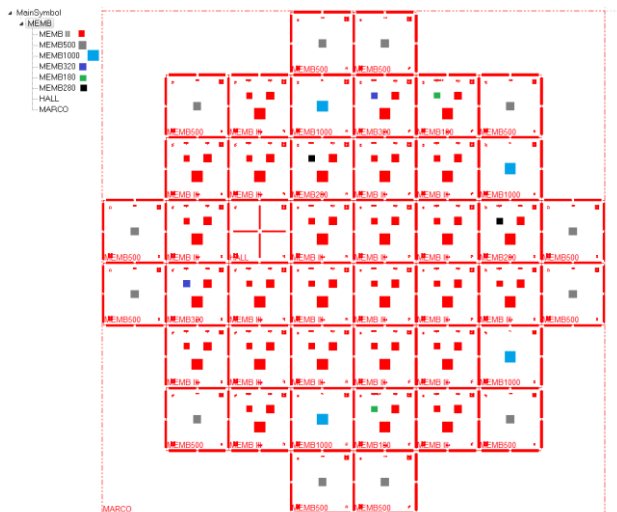


Figure 3. Transitions of two TES of size 150 μm, with design A, with and without banks (ZTES26 and ZTES28 respectively). These TESs were fabricated individually and independently; their similar transitions and characteristics (see TN8.6b) evidence the achievable fabrication control.



Figures 4. Masks for TES with design B: membrane mask (left) and chip design (right).

	<p>WP6 Detectors</p> <p>WP6.2. X-ray sensors</p> <p><i>WP6.2b Mo/Au pixels</i></p>	<p>Doc. no.: CSIC AHEAD Report WP6.2b-fab</p> <p>Issue : draft 1.0</p> <p>Date : 14/5/2018</p> <p>Page : 8 of 18</p>
		

Chips over the wafer incorporated TES of different geometries and sizes; square TESs with sizes ranging from 50 μm to 240 μm were included, and also two rectangular ones of sizes 100x140 μm and 100x225 μm .

The wiring in design B was initially of Nb, as in design A; however, it was changed to Mo/Nb because of the upgrade of fabrication procedure (described in next section). The T_c of used Mo/Nb wires (thicknesses 55 and 150 nm respectively) is nearly identical to that of Nb wires ($\sim 8.6\text{-}8.8$ K).

Normal metal structures, which were considered as a possibility to incorporate, have been finally not incorporated because of the rather low values of excess noise of TES without them (see accompanying report on device test [AD1]).

2.3. TES fabrication

2.3.1. Bilayer deposition

The Mo layer and the 15 nm-thick Au protecting layer are deposited in a UHV chamber equipped with a confocal magnetron sputtering system (Fig. 5). The chamber allows 5 different 2" targets, supplied either with DC or RF power sources, and contains a rotating 4" sample holder, designed to improve homogeneity of the deposited films. The working distance is 12 cm; base pressure is $< 5 \cdot 10^{-8}$ Torr. Targets with purity 99.95 % for Mo, Au and Nb are used. Table 4 summarizes deposition conditions of the three elements; these deposition conditions had been developed and optimized prior to the beginning of this WP.

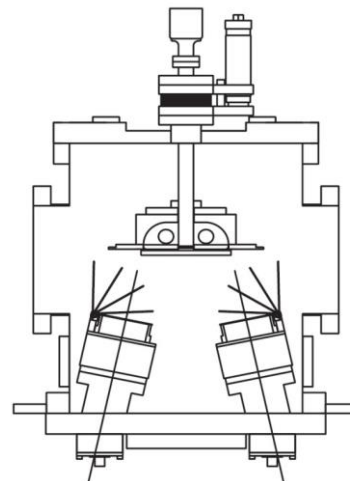


Figure 5. Sputtering chamber: planar view of the 2" guns (left) and schematics of the cross section (right).

	WP6 Detectors WP6.2. X-ray sensors <i>WP6.2b Mo/Au pixels</i>	Doc. no.: CSIC AHEAD Report WP6.2b-fab Issue : draft 1.0 Date : 14/5/2018 Page : 9 of 18
		

Material	Technique	Parameters	Deposition rate (nm/min)
Mo	RF sputtering	RT, 3 mTorr Ar, 260 W	9.8
Au	DC sputtering	RT, 3 mTorr Ar, 60 W	11.3
Au	ebeam evaporation	RT, 5.3 kV, 70 mA	13
Nb	DC sputtering	RT, 3 mTorr Ar, 160 W	7.9

Table 4. Deposition technique, conditions and rates of the three materials required for TES fabrication.

2.3.2. TES fabrication procedure

Table 5 describes the process of TES fabrication and membrane opening. Fig. 6 illustrates the whole procedure. Resist AZ6632 was removed from market during the work in this WP and was substituted by ECI3027.

Step	Title	Material	Technique
1	Deposition of MoAu bilayer in UHV	+ Mo [tbdnm]/Au [15nm]	Room temperature RF magnetron sputtering (Mo)/ DC magnetron sputtering (Au)
2	Ex-situ deposition of Au	+ Au [tbd nm]	e-beam
3	Positive resist pattern/ back side	+ AZ6632/ECI3027	spinner
4	Back Si ₃ N ₄ etching /back side	- Si ₃ N ₄	RIE with SF ₆
5	Resist removal/back side	- AZ6632/ECI3027	DMSO, 80°C, DI water
6	Positive resist pattern -TES	+ AZ6632/ECI3027	spinner
7	Definition of TES area	- Mo/Au	Dry etching of Au
8	Resist removal	- AZ6632/ECI3027	DMSO, 80°C, DI water
9	Deposition of Nb layer	+ Nb [150 nm]	DC magnetron sputtering
10	Positive resist pattern -WIRE	+ AZ6632/ECI3027	spinner
11	Definition of wiring	+ Mo/Nb	RIE with SF ₆
12	Resist removal	- AZ6632/ECI3027	DMSO, 80°C, DI water
13	Membrane opening	- Si	Wet etching by KOH, 80°C

Table 5. TES fabrication and membrane opening.



WP6 Detectors

WP6.2. X-ray sensors

WP6.2b Mo/Au pixels

Doc. no. : CSIC AHEAD Report WP6.2b-fab

Issue : draft 1.0

Date : 14/5/2018

Page : 10 of 18

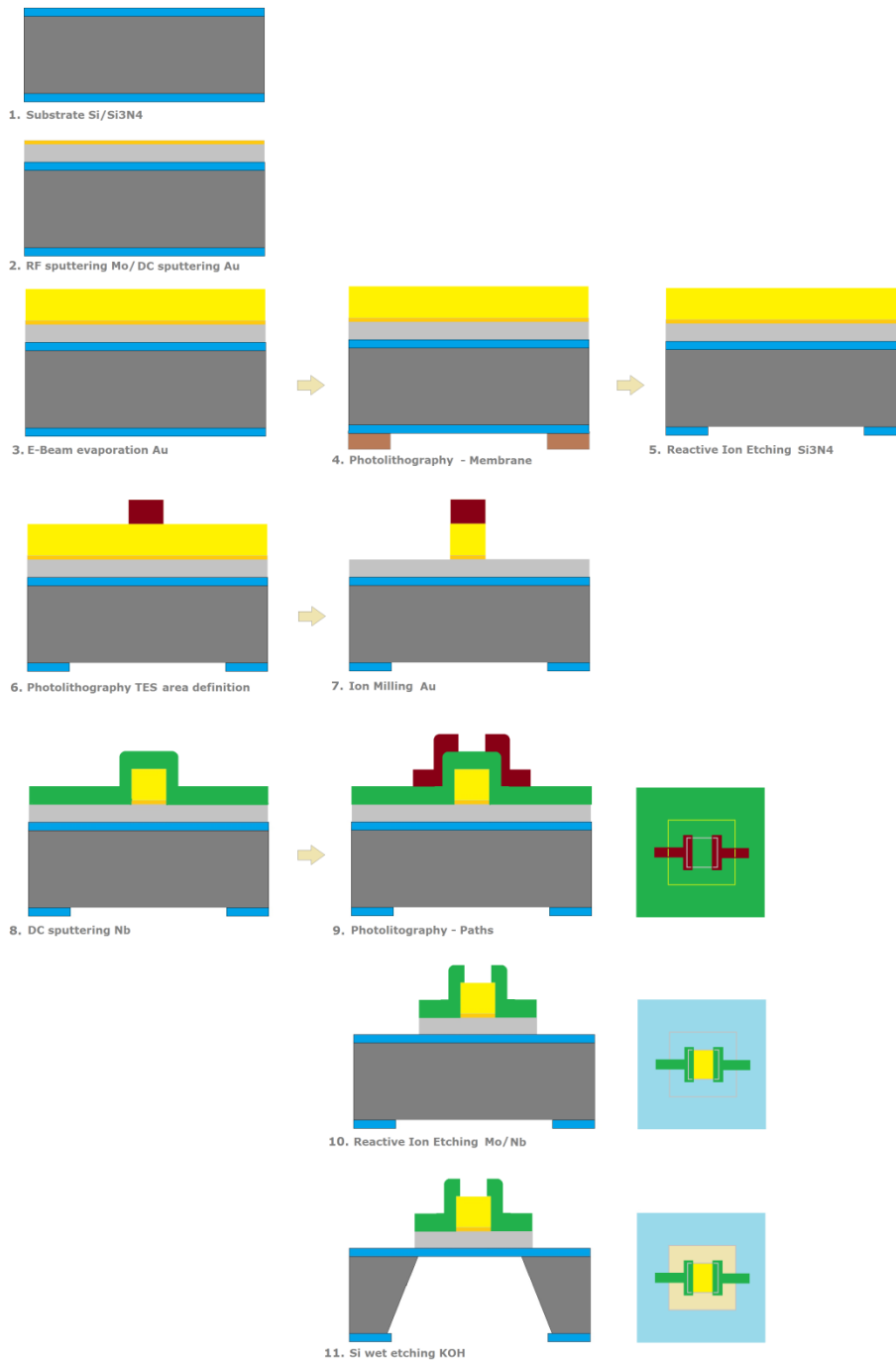
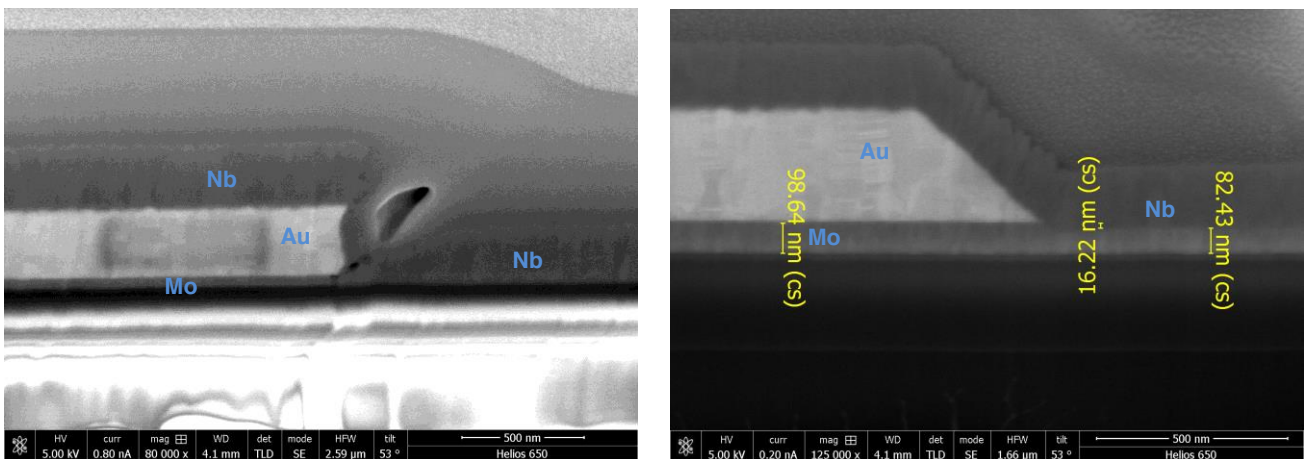


Figure 6. TES fabrication procedure.

	<p>WP6 Detectors</p> <p>WP6.2. X-ray sensors</p> <p>WP6.2b Mo/Au pixels</p>	<p>Doc. no.: CSIC AHEAD Report WP6.2b-fab</p> <p>Issue : draft 1.0</p> <p>Date : 14/5/2018</p> <p>Page : 11 of 18</p>
		

During the work within this project the fabrication process evolved, as a result of a careful study of the Mo/Au edge profiles obtained by different techniques and their impact on the quality, reproducibility and yield of the devices. Figs.7 display typical images obtained by SEM on sections carried out by FIB on the zone near the Mo/Au edge and contact to the pad, using (a) the initial fabrication procedure, which included wet etching of the Mo/Au bilayer, and (b) the present procedure, described in full in next section. The main changes and outcomes are the following:

- Substitution of Nb wires by Mo/Nb wires in order to improve the contact between the pad on the bilayer and the wire. The use of Nb alone resulted in non-conformal/irregular coating of the bilayer edge, which caused contact problems and a lack of reproducibility.
- The membranes opening by wet etching at the end of the fabrication procedure improved substantially reproducibility.
- Use of dry etching, which has resulted in controlled sloped edges of Mo/Au bilayer.



Figures 7. SEM images of TES cross-sections close to the Mo/Au edge and pad, obtained by FIB: on the left, a TES fabricated by the initial procedure; on the right, a TES produced by the upgraded, presently used, procedure described on Table 5.

Figs. 8 and 9, displaying an image of a TES from batch 2 and the transitions of two TESs from a chip of the same batch, are illustrative of the quality of the devices fabricated.

	<p>WP6 Detectors</p> <p>WP6.2. X-ray sensors</p> <p>WP6.2b Mo/Au pixels</p>	<p>Doc. no.: CSIC AHEAD Report WP6.2b-fab</p> <p>Issue : draft 1.0</p> <p>Date : 14/5/2018</p> <p>Page : 12 of 18</p>
		

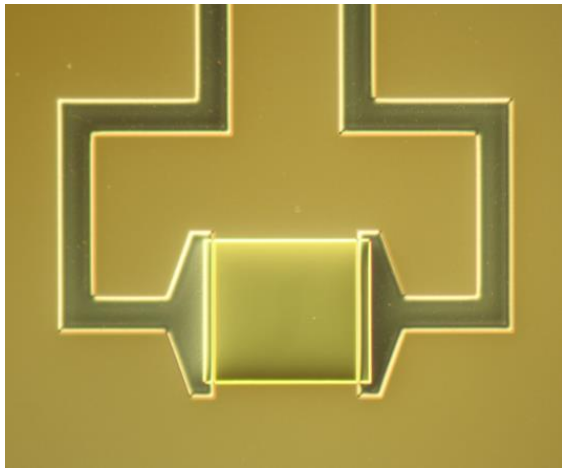


Figure 8. Optical micrograph of a TES with design B.

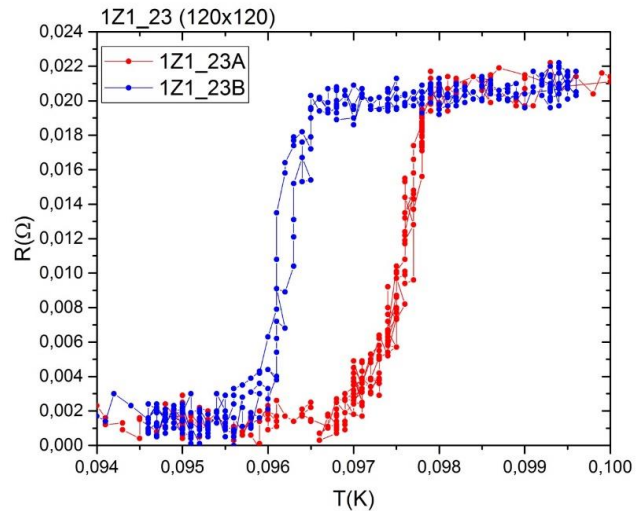


Figure 9. Resistive transition of two TES without absorber, corresponding to a single chip and fabricated on neighboring membranes of different area: $250 \times 250 \mu\text{m}^2$ (A) and $1000 \times 1000 \mu\text{m}^2$ (B).

3. X-ray absorbers

3.1. Electrodeposition of Bi and Au

Absorbers made of Bi, Au and Au/Bi were fabricated by electrodeposition, using a three-electrode cell configuration (Fig.10). The substrate or wafer containing TES was used as working electrode, while a 10x10cm Pt grid was the counterelectrode and an Ag/AgCl electrode acted as the reference electrode. Table 6 displays the electrochemical deposition parameters for both Bi and Au, for the specified thicknesses. All electrodepositions were performed using constant current conditions.

During the development of the electrodeposition processes, which is not described here, it was found that sensibly different results are obtained when using surfaces with or without resists (required for absorber patterning), in terms of material morphology, which necessarily translate to different functional properties. Bismuth faced two additional difficulties: its electrodeposition is quite different on the seed layer (by thermal or e-beam evaporation) and on electrodeposited Au because of underpotential electrodeposition effects; also, the deposition parameters of Bi do not scale with area, for small areas. Because of these two reasons electrodeposited Bi absorbers (in presence of resists) cannot be considered optimized at this stage and their development continues; data and images reported in the following pages correspond to the best conditions so far. Optimization of Au is in a more advanced stage, although some refining will be required and come along the capability to characterize pulse detection (setup in progress).

	<p>WP6 Detectors</p> <p>WP6.2. X-ray sensors</p> <p>WP6.2b Mo/Au pixels</p>	<p>Doc. no.: CSIC AHEAD Report WP6.2b-fab</p> <p>Issue : draft 1.0</p> <p>Date : 14/5/2018</p> <p>Page : 13 of 18</p>
		

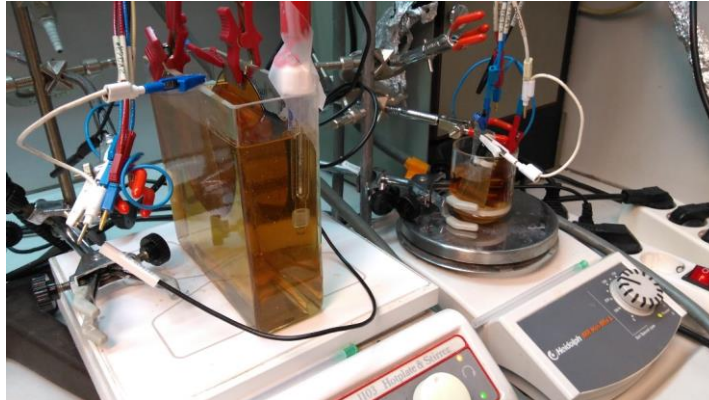


Figure 10. Setup for electrochemical deposition of Bi or Au on wafers.

Material	Thickness (μm)	Electrolyte	Temperature	Stirring (rpm)	I (mA/cm^2)	Q (C/cm^2)
Bi	4	NB semiplate Bi 100	Room Temp	500	-3.6*	-40*
Au	1.4	Technigold 25 ES RTU	55°C	300	-1.5	-1.6
Bi over electrodeposited Au	4	NB semiplate Bi 100	Room Temp	500	-2.4**	-14**

Table 6. Electrochemical constant current deposition parameters for both materials, to achieve the indicated thicknesses.

* The current density and final delivered charge values for Bi deposited on the Au seed layer correspond to the best conditions when using a quarter (1/4) of the wafer: refining conditions on full wafers is in progress and not complete, but both optimal I and Q are expected to be significantly lower.

** Present conditions, not yet optimal; further optimization and studies in progress.

Nonetheless, we have performed a study and optimization of the resistivity of Bi and Au films electrodeposited on areas of several cm^2 , free of resists, covered with a seed layer of 10nm-thick thermally evaporated Au. For Bi, the best obtained resistance ratio $\text{RRR}=\text{R}(300\text{K})/\text{R}(2\text{K})$ is $\text{RRR}\sim 1$, with minimum resistivity values $200\ \mu\Omega\text{cm}$ for $6\ \mu\text{m}$ -thick films (Fig. 11), which is quite close to state of the art [RD7]. The best RRR obtained for electrodeposited $1\ \mu\text{m}$ -thick Au films is 9.3, indicating that there is still room for improvement.

	<p>WP6 Detectors WP6.2. X-ray sensors WP6.2b Mo/Au pixels</p>	<p>Doc. no.: CSIC AHEAD Report WP6.2b-fab Issue : draft 1.0 Date : 14/5/2018 Page : 14 of 18</p>
		

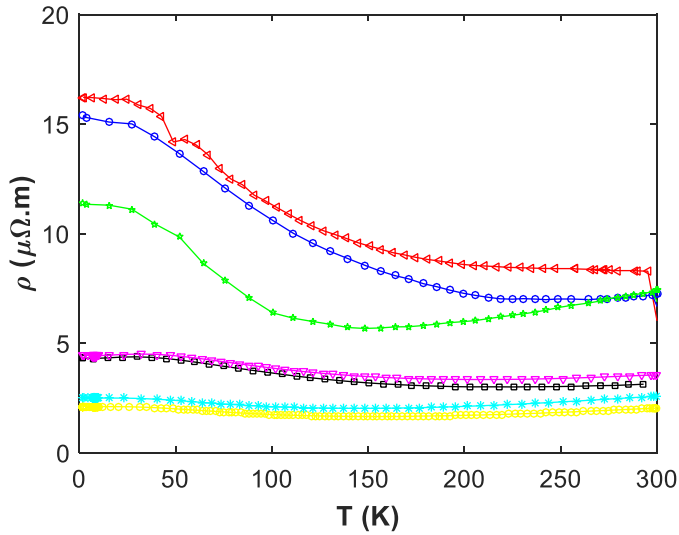
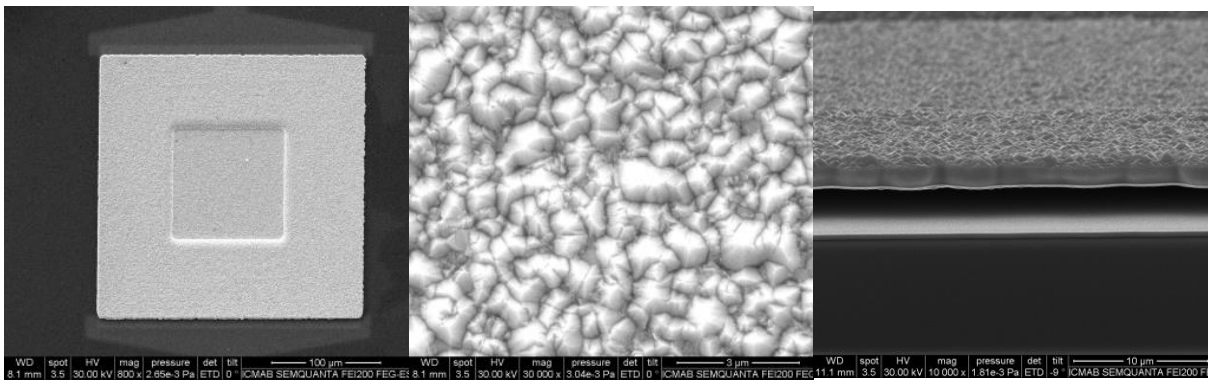


Figure 11. Temperature dependence of resistivity of several Bi films (6 μm thick), obtained under different electrodeposition conditions and electrolytes. For details see [RD7].



Figures 12. SEM images of an electroplated Au absorber, fabricated at constant current densities of -1.5 mA/cm^2 . Au thickness is $1.5 \mu\text{m}$ in this case; similar absorbers and morphologies are obtained for $2.5 \mu\text{m}$.

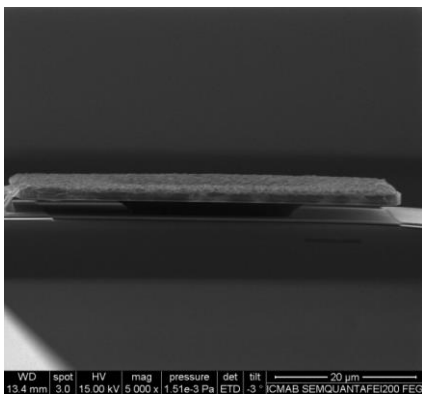


Figure 13. Mushroom-shaped $1.4 \mu\text{m}$ thick Au absorber with dimensions $20 \mu\text{m}$ (foot) and $50 \mu\text{m}$ (hat), on a $50 \mu\text{m}$ TES.

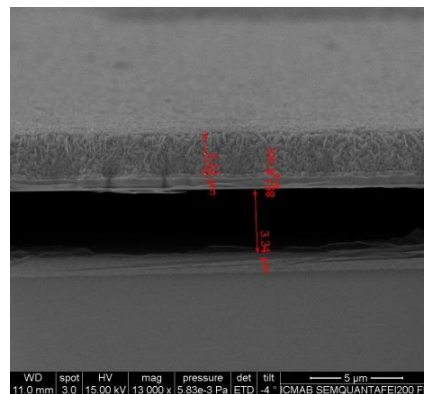
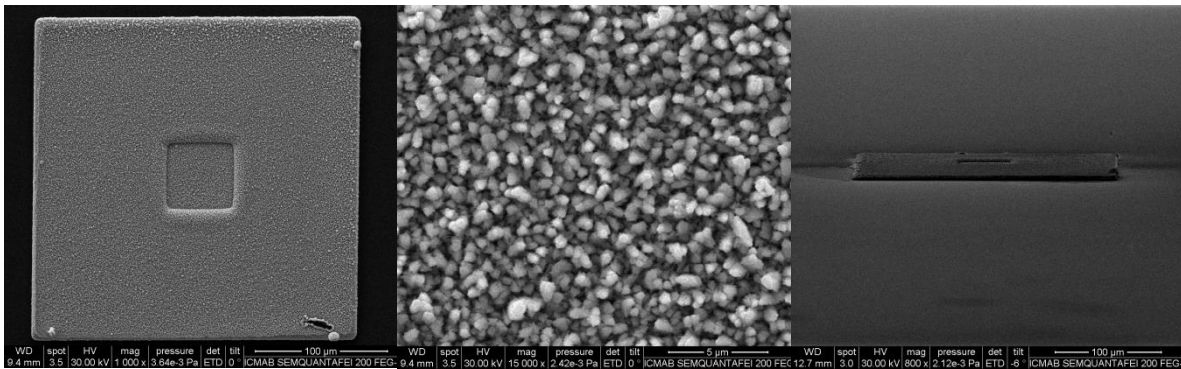


Figure 14. Bi/Au mushroom absorber electroplated on a wafer quarter; Au and Bi were deposited respectively using current densities of -1.5 and -2.5 mA/cm^2 .

	<p>WP6 Detectors WP6.2. X-ray sensors <i>WP6.2b Mo/Au pixels</i></p>	<p>Doc. no.: CSIC AHEAD Report WP6.2b-fab Issue : draft 1.0 Date : 14/5/2018 Page : 15 of 18</p>
		



Figures 15. SEM images of electroplated Bi deposited on electroplated 1.4μm-thick Au, using a constant current density -2.6 mA/cm^2 .

3.2 Absorber design

Most fabricated absorbers, both with TES designs A and B, did correspond to central absorbers on the TES, either blocks or mushrooms, the latter have stems $\sim 3 \mu\text{m}$ high of variable width. Typical areas were $50 \times 50 \mu\text{m}^2$ and $100 \times 100 \mu\text{m}^2$. Later, masks for TES with design B included mainly mushroom-shaped absorbers with different stem and hat areas (hats between 50×50 and $240 \times 240 \mu\text{m}^2$), some blocks of the same areas and also two other designs with reduced contact area with the TES: a cantilevered $240 \times 240 \mu\text{m}^2$ square with either 5 square pillars or a T-shaped basis (Fig.16). Figures 17 display images of Au absorbers with these two designs.

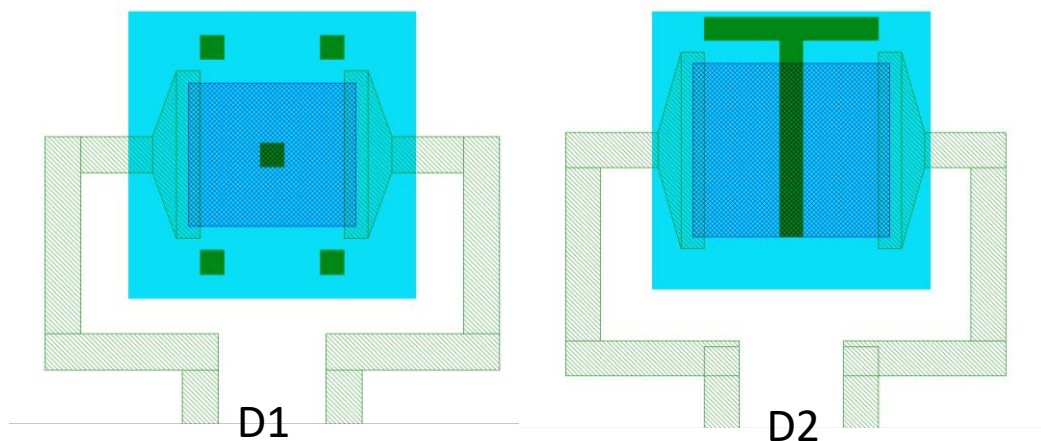
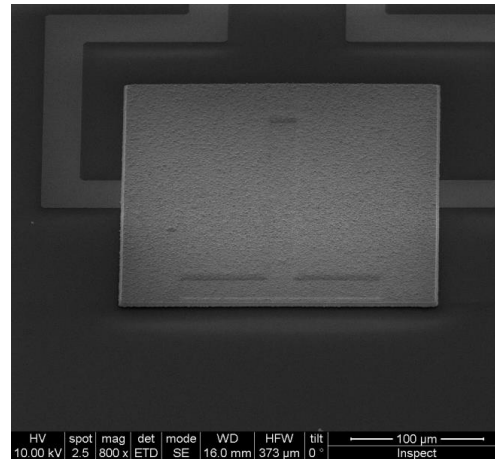
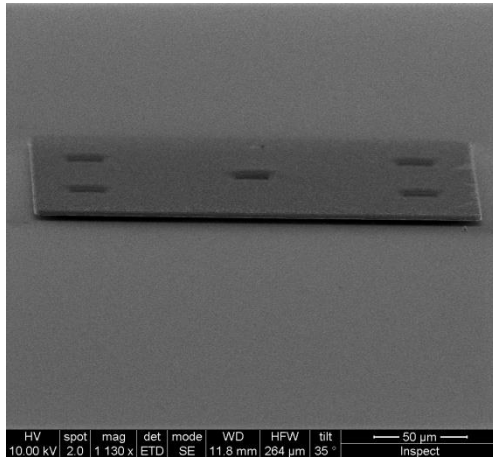


Figure 16. The two absorber designs with reduced contact area to the TES, D1 and D2. The hat is $240 \mu\text{m}$ wide in both cases; the pillars in D1 and the lines of the T-shaped stem in D2 are $20 \mu\text{m}$ wide.

	<p>WP6 Detectors</p> <p>WP6.2. X-ray sensors</p> <p>WP6.2b Mo/Au pixels</p>	<p>Doc. no.: CSIC AHEAD Report WP6.2b-fab</p> <p>Issue : draft 1.0</p> <p>Date : 14/5/2018</p> <p>Page : 16 of 18</p>
		



Figures 17. Two images of cantilevered 240 μ m wide Au absorbers: on the left, over 5 pillars, and on the right with a T-shaped stem, on a TES of smaller area.

3.3 Absorber fabrication procedure

The absorber fabrication procedure is detailed in Table 7 and Fig. 18.

Step	Title	Material	Technique, process
1	Positive resist pattern (R1)-absorber foot	ECI3027 (3 μ m)	3000 rpm, 60'' + 2' soft bake 100°C + soft contact, 20'' exposure 250 mJ/cm ² + 65' development AZ826MIF:H ₂ O (1:1) + 2' hard bake 120°C + N ₂ extraction (15'' exposure, 1' wait, 30'' exposure, 2' wait, 1' exposure, 10' wait, 2' exposure) + Low power O ₂ plasma cleaning – 1'
2	Deposition of seed layer	+ Ti [5nm]/Au [120 nm]	e-beam evaporation
3	Positive resist pattern (R2)	AZ9260 (8.4 μ m)	3000 rpm, 60'' + 15' soft bake 80°C + Hard contact, 60'' exposure 750 mJ/cm ² + Development AZ826MIF 210'' + Low power O ₂ plasma cleaning – 1'
4	Deposition of absorber (Bi and/or Au)	+ Au [μ m] and/or Bi	Electrochemical deposition
5	Resist 2 removal	-AZ9260	Acetone-RT, 60' + IPA clean
6	Seed layer removal	-Ti/Au	Clean surface with O ₂ plasma – 1' + Au dry etching (ion milling), 6x (1' etch + 1' wait) + Ti RIE etching 40''
7	Resist 1 removal	- ECI3027	Plasma O ₂ resist etching – 2' + NMP stripper – 40°C, 6' + Acetone/IPA/ethanol cleaning + Natural drying on air

Table 7. Absorber fabrication procedure.

	<p>WP6 Detectors</p> <p>WP6.2. X-ray sensors</p> <p>WP6.2b Mo/Au pixels</p>	<p>Doc. no.: CSIC AHEAD Report WP6.2b-fab</p> <p>Issue : draft 1.0</p> <p>Date : 14/5/2018</p> <p>Page : 17 of 18</p>
		

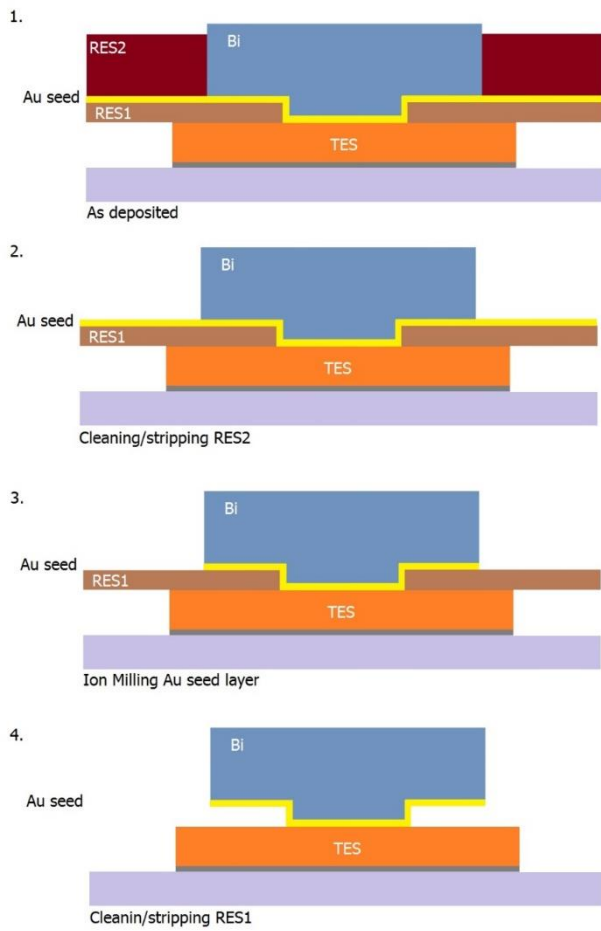


Figure 18. Absorber fabrication procedure.

	<p>WP6 Detectors</p> <p>WP6.2. X-ray sensors</p> <p><i>WP6.2b Mo/Au pixels</i></p>	<p>Doc. no.: CSIC AHEAD Report WP6.2b-fab</p> <p>Issue : draft 1.0</p> <p>Date : 14/5/2018</p> <p>Page : 18 of 18</p>
		

4. CONCLUSIONS

Mo/Au-based TES have been fabricated on silicon nitride membranes of different area and thickness:

- With sizes between 50x50 and 240x240 μm .
- Most square, but also two rectangular ones, with sizes 100x140 and 100x225 μm .
- With and without banks, in both cases with excellent transition widths and similar performances.
- With $T_c \sim 100$ mK.
- With typical transition widths ~ 1 -2 mK.
- With $R_n \sim 10$ -30 $\text{m}\Omega$, depending on the TES shape and the presence/absence of banks.

Even more, a calibration of the T_c of bilayers of different thickness has allowed to determine thicknesses to fabricate TES with $T_c \sim 100$ mK and higher resistance (lower thickness), so that the R_n accessible is roughly $R_n \sim 10$ -40 $\text{m}\Omega$ (with present masks and designs).

Some of the devices included also electrodeposited X-ray absorbers:

- Made of Bi (4-6 μm), Au (1.4 μm) and Au/Bi (same thicknesses)
- Absorber shapes were mainly central mushrooms and central square blocks. However, other two designs with reduced contact area with the TES have also been fabricated.
- The produced absorbers are well adhered and well defined, and morphology of electroplated Au is good enough. However, two issues require further work:
 - Improvement of Bi morphology.
 - Further functional characterization and refinement when the characterization setup will allow pulse detection and spectral resolution measurement.

5. FUTURE WORK

Development of Mo/Au TES pixels will follow along the following lines:

- Fabrication of smaller sensors
- Optimization of X-ray absorber designs
- Design and fabrication of small arrays

 <p>AHEAD</p>	WP6 Detectors	
 <p>CONSEJO SUPERIOR DE INVESTIGACIONES CIENTÍFICAS</p>	WP6.2. X-ray sensors <i>WP6.2b Mo/Au pixels</i>	Doc. no.: CSIC AHEAD Report WP6.2b-test Issue : draft 1.0 Date : 14/05/2018 Page : 1 of 36

Title: report WP6.2b, Mo/Au TES test

Prepared by : Lourdes Fàbrega, Agustín Camón, Carlos Pobes

	<p>WP6 Detectors</p>	<p>Doc. no.: CSIC AHEAD Report WP6.2b-test</p>
	<p>WP6.2. X-ray sensors</p> <p><i>WP6.2b Mo/Au pixels</i></p>	<p>Issue : draft 1.0</p> <p>Date : 14/05/2018</p> <p>Page : 2 of 36</p>

Contents

ABBREVIATIONS AND ACRONYMS	3
APPLICABLE DOCUMENTS	3
REFERENCE DOCUMENTS	3
1. SUMMARY	4
2. Devices tested	4
3. DC Dark Characterization description	6
3.1. R(T) measurements	6
3.2. I-V curves	6
3.3. Complex impedance	11
3.4. Noise	17
4. Analysis of results	22
4.1. Evolution of main TES parameters as a function of bias and T_{bath}	23
4.2. Effect of banks	33
5. CONCLUSIONS	35
6. FUTURE WORK	35

	<p>WP6 Detectors</p> <p>WP6.2. X-ray sensors</p> <p><i>WP6.2b Mo/Au pixels</i></p>	<p>Doc. no.: CSIC AHEAD Report WP6.2b-test</p> <p>Issue : draft 1.0</p> <p>Date : 14/05/2018</p> <p>Page : 3 of 36</p>
		

ABBREVIATIONS AND ACRONYMS

Item	Meaning
------	---------

BCS	Bardeen-Cooper-Schrieffer (theory)
NEP	Noise Equivalent Power
RRR	Residual Resistance Ratio
STB	Single Thermal Block
TES	Transition Edge Sensor
WP	Work Package

APPLICABLE DOCUMENTS

[AD#]	Document reference	Title
-------	--------------------	-------

[AD1]	CSIC AHEAD Report WP6.2b-fab	Mo/Au pixel fabrication
-------	------------------------------	-------------------------

REFERENCE DOCUMENTS

[RD#]	Reference
-------	-----------

[RD1]	K.D.Irwin, C.C.Hilton, "Transition-Edge Sensors in Cryogenic Particle Detection", edited by C.Enss, Springer-Verlag, Berlin Heidelberg, Topics in Applied Physics, vol. 99, pp.63-149 (2005)
[RD2]	D.A.Bennett et al., "Resistance in transition-edge sensors: A comparison of the resistively shunted junction and two-fluid models", Phys. Rev. B87, 020508(R) (2013)
[RD3]	C.Pobes et al., "Development of cryogenic X-ray detectors based on Mo/Au Transition Edge Sensors", IEEE Trans. Appl. Supercond. 27, 2101505 (2017)
[RD4]	M.Galeazzi, "Fundamental Noise Processes in TES devices", IEEE Trans. Appl. Supercond. 21, 267 (2011)
[RD5]	J.N.Ullom et al., "Characterization and reduction of unexplained noise in superconducting transition-edge sensors", Appl. Phys. Lett. vol 84, 4206 (2004)
[RD6]	Mark A. Lindeman et al. "Impedance measurements and modeling of a transition edge-sensor calorimeter". Rev. Sci. Instrum. 75, 1283 (2004)

	<p>WP6 Detectors</p> <p>WP6.2. X-ray sensors</p> <p><i>WP6.2b Mo/Au pixels</i></p>	<p>Doc. no.: CSIC AHEAD Report WP6.2b-test</p> <p>Issue : draft 1.0</p> <p>Date : 14/05/2018</p> <p>Page : 4 of 36</p>
		

1. SUMMARY

This document describes the results of the characterization of several Mo/Au based TES microcalorimeters carried out by CSIC. It begins with the list and description of the characterized devices (section 2), followed by a summary of the characterization setup and the procedures to extract TES parameters (section 3). Section 4 is devoted to the analysis of results and comparison between devices. It follows with a list of the main conclusions (section 5) and lines of future work (section 6). Description of the fabrication process and designs are the subject of a separate document [AD1].

2. Devices tested

Tables 1 and 2 summarize the main characteristics of the measured TESs. Two designs are considered, one with a single device per chip and processed individually (Design A), which corresponds to the ZTESxx devices and one with three devices per chip and processed in a single wafer (Design B), corresponding to TESs identified as 1Zx. As can be seen, different widths and sizes of SiN membranes have been tested as well as different bilayer dimensions. It has to be noted that in Design A, bilayer area refers to the full bilayer size, which means that the effective area is 20 μm shorter due to the Niobium reading pads and 20 μm thinner due to the banks (in those devices which do have them). This was modified in Design B where the bilayer area already refers to effective area. This difference explains the different R_n values for similar devices.

Design A	ZTES13	ZTES18	ZTES20	ZTES25	ZTES26	ZTES28
Membrane thickness (μm)	0.5	0.5	0.5	0.5	1	1
Membrane size (mm^2)	1x1	0.5x0.5	0.5x0.5	0.5x0.5	0.5x0.5	0.5x0.5
Bilayer area (μm^2)	200x200	150x150	100x100	200x200	150x150	150x150
Banks	Yes	Yes	Yes	Yes	Yes	No
Absorber	No	No	No	No	No	No
R_n ($\text{m}\Omega$)	14.9	12.5	8.9	15	13.5	16
T_c (mK)	115	91	90	110	109	113

Table 1. Design parameters, normal resistance R_n and critical temperature T_c of tested devices with design A.

	<p>WP6 Detectors</p> <p>WP6.2. X-ray sensors</p> <p><i>WP6.2b Mo/Au pixels</i></p>	<p>Doc. no.: CSIC AHEAD Report WP6.2b-test</p> <p>Issue : draft 1.0</p> <p>Date : 14/05/2018</p> <p>Page : 5 of 36</p>
		

Design B	1Z1_54A	1Z1_23A	1Z1_54B	1Z2_35A	1Z10_45B
Membrane thickness (μm)	1	1	1	0.5	0.5
Membrane size (mm^2)	0.25x0.25	0.25x0.25	1.0x1.0	0.25x0.25	1.0x1.0
Bilayer area (μm^2)	100x140	120x120	100x140	100x140	120x120
Banks	No	No	No	No	No
Absorber	No	No	6 μm -thick Bi Mushroom 100/50 μm	6 μm -thick Bi Mushroom 100/50 μm	Au 1.4 μm -thick, mushroom 100/50 μm
R_N (mΩ)	29	23	29	26.7	11.8
T_c (mK)	98	97	103	129	90.5

Table 2. Design parameters, normal resistance R_N and critical temperature T_c of tested devices with design B.

First devices characterized (design A) included banks, which were later suppressed because improvements in fabrication procedure [AD1] allowed obtaining TES with nearly identical performances, as we shall see upon comparison of ZTES26 and ZTES28.

It must be taken into account that the TES characterization advanced in parallel with the development of absorber fabrication procedure, which was initially focused on Bi blocks and mushrooms. Since the heat capacity of Bi is much lower than that of Au and our TES have a thick Au layer, these absorbers were not expected to add any significant C to that of bare TESs; therefore, the dark characterization of these devices was mostly meant to verify that the absorber presence and fabrication procedure were not detrimental to the TES performances. The development of Au absorbers changed this, since the Au block adds a heat capacity of the order of or larger than that of the TES, thereby also changing significantly τ_{eff} . However, the absence of spectral resolution measurements limit also the characterization of other effects of the absorber presence.

3. DC dark characterization measurements

The devices are characterized in a dilution refrigerator (Kelvinox MX40, from Oxford Instruments), with field screening, base temperature of 27 mK and a refrigeration power of 80 mW at 100 K. The set-up allows housing of 7 samples: 6 to measure $R(T)$ and 1 in a separate holder with a dedicated SQUID, for full dark characterization. Therefore, characterization usually proceeds in two steps. In a first cool down the $R(T)$ of the device is measured. In a

	<p>WP6 Detectors</p> <p>WP6.2. X-ray sensors</p> <p>WP6.2b Mo/Au pixels</p>	<p>Doc. no.: CSIC AHEAD Report WP6.2b-test</p> <p>Issue : draft 1.0</p> <p>Date : 14/05/2018</p> <p>Page : 6 of 36</p>
		

second cool down the dark characterization of a device (selected from previous measured $R(T)$) is performed: it includes measurements of IV curves, complex impedances $Z(w)$ and noise at several operating points (different I_{bias} and bath temperatures T_{bath}) from which the main dynamic parameters are obtained. According to the Wp6.2b workplan, no spectral resolution measurements were carried out, although they are envisaged in the near future.

3.1 $R(T)$ measurements

$R(T)$ is measured with an AVS-47 bridge with the minimum range and excitation (on the order of a few μA) to ensure the minimum possible dissipated power in the device. From the measured transition we obtain the R_n as the constant resistance value (residual resistance) before the beginning of the superconducting drop, T_c as the temperature of resistance onset and transition width ΔT as the temperature difference between 0% and 90% of R_n . Fig.1 shows a typical $R(T)$ transition of our devices.

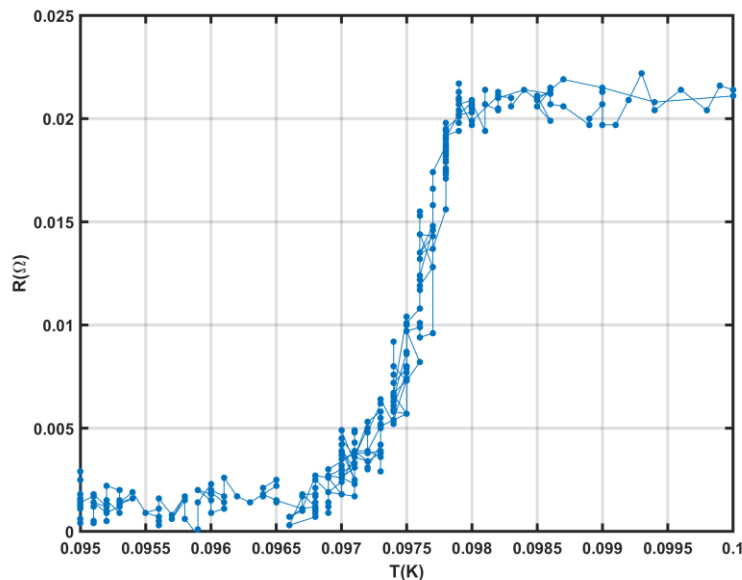


Figure 1. Resistive transition of one of the devices. Data depicted include thermal sweep up and down.

3.2 I-V curves

The basic set-up for IV measurements is sketched in Fig. 2 The TES is biased with an external current source through a parallel shunt resistance, R_{sh} , which provides an effective voltage bias and therefore a negative electrothermal feedback allowing stable operation inside the transition; the value of R_{sh} used in all measurements is 2 m Ω , which poses some limitations to the lowest achievable % R_n for TES with low R_n , as shall be seen in Section 4. The current going through the TES is measured with a SQUID (series C6 provided by PTB) working in Flux Locked

	<p>WP6 Detectors</p> <p>WP6.2. X-ray sensors</p> <p>WP6.2b Mo/Au pixels</p>	<p>Doc. no.: CSIC AHEAD Report WP6.2b-test</p> <p>Issue : draft 1.0</p> <p>Date : 14/05/2018</p> <p>Page : 7 of 36</p>
		

Loop (FLL) mode. The SQUID output is fed to a precision multimeter which, together with the bias current, is read with a control PC in order to build the experimental IV curves. From these values of I_{bias} - V_{out} pairs and the known circuit parameters (R_{shunt} , $R_{parasitic}$, $R_{feedback}$ and mutual inductances) the TES current, voltage, resistance and power are obtained (Fig.3). The equations used for the calculations are:

$$I_{TES} = \frac{V_{OUT} M_f}{M_{in} R_f}, \quad \left[\frac{1}{Min} = 24.1 \frac{\mu A}{\Phi_0}, \frac{1}{Mf} = 75 \frac{\mu A}{\Phi_0} \right] \quad (1.a)$$

$$R_{par} = \left(\frac{I_{bias}}{I_{TES_S}} - 1 \right) R_{shunt} \quad (1.b)$$

$$R_n = \left(\frac{I_{bias}}{I_{TES_N}} - 1 \right) R_{shunt} - R_{par} \quad (1.c)$$

$$V_{TES} = (I_{bias} - I_{TES}) R_{shunt} - I_{TES} R_{par} \quad (2.a)$$

$$P_{TES} = V_{TES} I_{TES} \quad (2.b)$$

$$R_{TES} = V_{TES} / I_{TES} \quad (2.c)$$

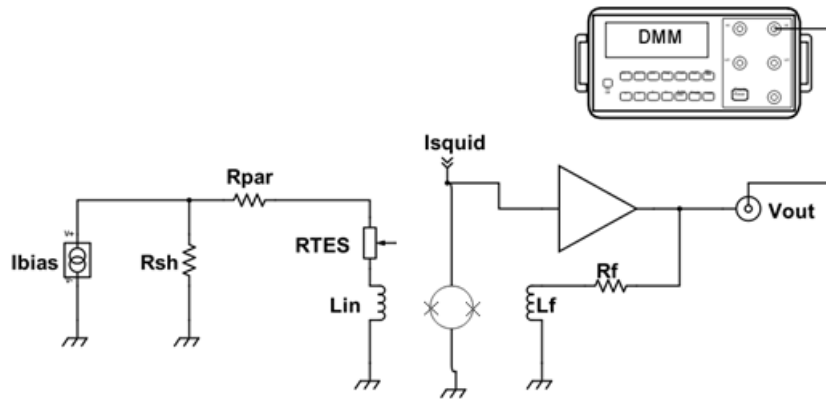


Figure 2. Electrical scheme of the I-V measurement setup.

The IV curve is acquired as follows. First, a bath temperature is selected and stabilized. Then, the TES is put into normal state with a current higher than the critical current of the TES, and finally a scan in I_{bias} is performed decreasing the current from around 500 μA to 0. The process is repeated both with positive and negative I_{bias} . The holder includes a coil with which a small magnetic field can be applied to compensate the trapped magnet field. In practice, our curves

	<p>WP6 Detectors</p> <p>WP6.2. X-ray sensors</p> <p>WP6.2b Mo/Au pixels</p>	<p>Doc. no.: CSIC AHEAD Report WP6.2b-test</p> <p>Issue : draft 1.0</p> <p>Date : 14/05/2018</p> <p>Page : 8 of 36</p>
		

seem to be quite symmetric as can be inferred by the slopes of the normal and superconducting states (of both polarities) intersecting at the origin (0,0) (see inset in Fig.3).

The above mentioned process is repeated for several bath temperatures which range from our lowest achievable temperature of around 30mK up to and above the critical temperature of the TES. With this complete set of curves we proceed to determine the thermal conductance of the TES to the bath which should come from the SiN membrane. The equations involved are:

$$P(T_{bath}) = K [T_c^n - T_{bath}^n] \quad (3.1)$$

$$G(T) = \frac{dP(T)}{dT} = nKT^{(n-1)} \quad (3.2a)$$

$$G_0 = G(T_c) = nKT_c^{(n-1)} \quad (3.2b)$$

$$G_{100} = G(0.1) = nK(0.1)^{(n-1)} \quad (3.2c)$$

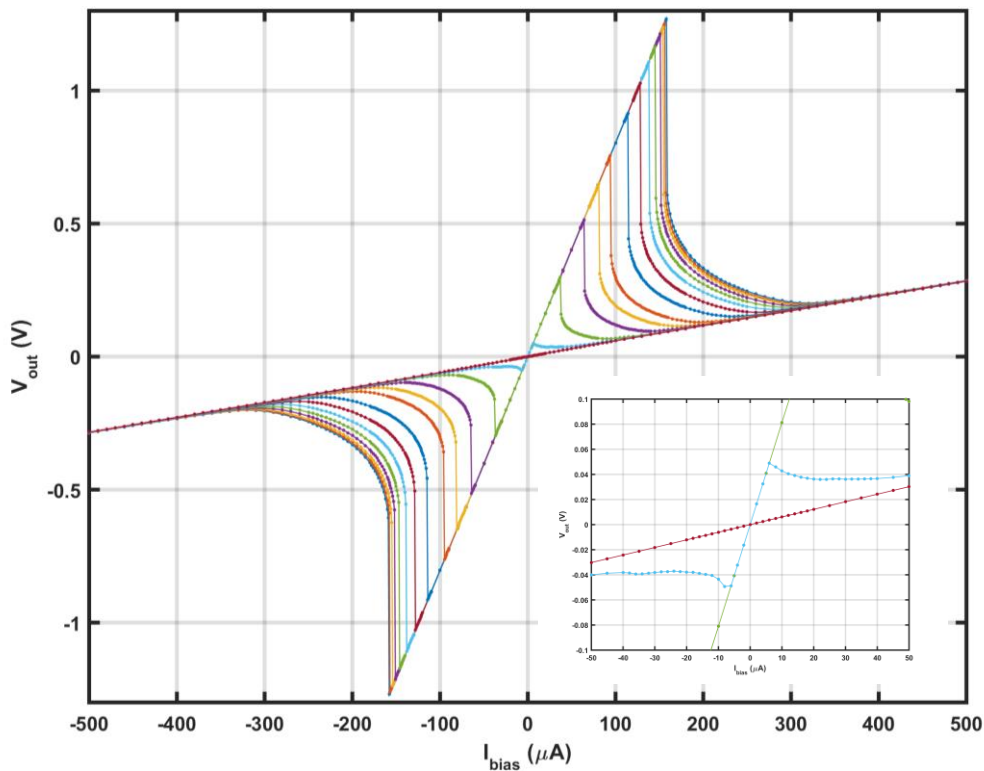


Figure3. Representative IV curves of one of the TES, with positive and negative polarities. Inset: zoom of the region close to origin.

	<p>WP6 Detectors</p> <p>WP6.2. X-ray sensors</p> <p>WP6.2b Mo/Au pixels</p>	<p>Doc. no.: CSIC AHEAD Report WP6.2b-test</p> <p>Issue : draft 1.0</p> <p>Date : 14/05/2018</p> <p>Page : 9 of 36</p>
		

The experimental data are fitted to expression (3.1) where it is assumed that the TES temperature is constant and equal to T_c . Even though T_c is known from previous $R(T)$ measurements, it is left as a free parameter for the fit. From the fitted parameters, the conductance at the operating temperature T_c (G_0) is obtained. In order to compare different TESs (where T_c may vary) we also calculate a normalized conductance at 100 mK which we call G_{100} (3.2c). The fact that the transition has a finite width implies that the TES temperature is not exactly constant along the transition. In order to estimate the possible systematic error introduced by this effect, we perform the fit for several points ($\%R_n$) along the transition and then get an estimate of how the fitted parameters vary along the transition. It should be noted that it is not the physical parameters which vary (in particular n and K are expected to be constant), but the results of the fit; therefore, the observed changes provide an estimate of the error in the determination of the thermal parameters from these fits. For robustness we also compare the result from the positive bias set and negative bias set. The result for a typical TES can be seen in Figs 4 and 5.

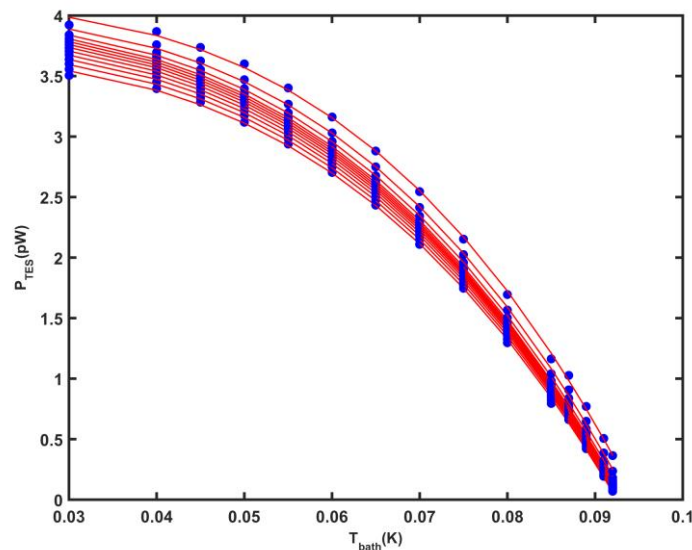
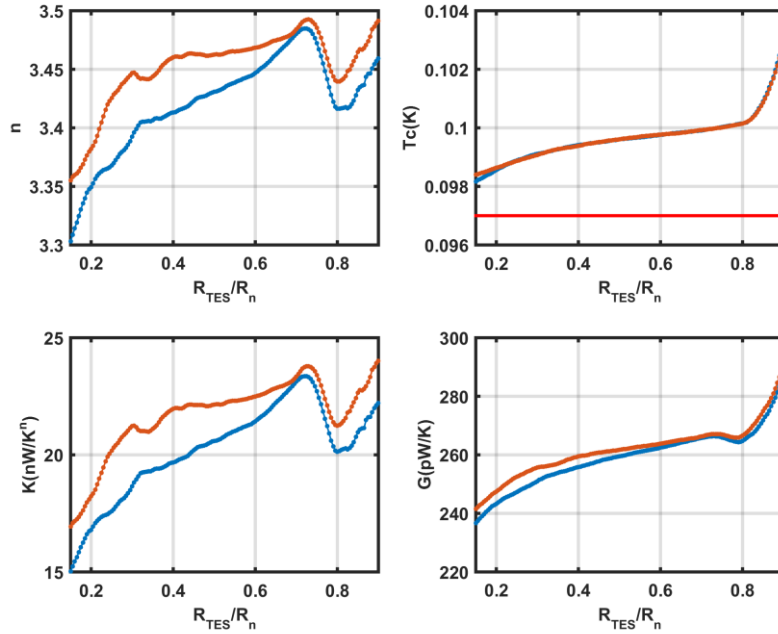


Figure 4. Fits $P(T_{bath})$ at different $\%R_n$ for a typical TES. The lines are fits to Eq.(3.1)

As can be seen, there is a systematic error in the estimate which may reach up to around 10% for the conductivity G . From Eqs.3 one can derive the sensitivity of G to variations in the other parameters, which is consistent with the observed results. As we mentioned, n and K should be constant along the transition. The fact that they vary may be an indication that the assumption of a constant T_{TES} is not completely valid. This has led us to consider more complicated models for the fit. For instance, one can assume a Ginzburg-Landau type relation between I_{TES} and T_{TES} in the transition and include this relation to allow for a varying T_{TES} . The obtained fits produce a new (n, K, G, T_c) set which is consistent with the ones obtained from the more simple fit of Eq. (3.1), within a few percent. Finally, simulations have also been made

	<p>WP6 Detectors</p>	<p>Doc. no.: CSIC AHEAD Report WP6.2b-test Issue : draft 1.0 Date : 14/05/2018 Page : 10 of 36</p>
	<p>WP6.2. X-ray sensors <i>WP6.2b Mo/Au pixels</i></p>	

in order to estimate the error in the parameters extracted from these fits in an independent way. For this, a TES with fixed n , K , T_c and $R(T, I)$ is considered and IV curves are simulated. The same algorithms used for real data are used for these simulated IVs. The results indicate that the naïve fit can underestimate the real (n , K , T_c) but again, just by a few percent. In short, detailed inspections have been performed in order to assess the robustness of our data analysis, an important requirement when comparing the performances of several TES. We conclude that there may be some systematic error in the estimate of G that may account up to a 10% in the error budget, which should be taken into account when comparing our devices.



Figures 5. Values of the fitted parameters (thermal exponent n , the thermal conductance G , conductivity K and the critical temperature T_c) obtained from the $P(T_{bath})$ fits, for positive (blue) and negative (orange) biases, for a typical TES. The horizontal red line in the T_c graph is the critical temperature extracted from the resistive transition ($R=0$ criterion).

For some of the TESs, measurements of their critical current at different bath temperatures have also been performed. For this purpose, bath temperatures near the critical temperature of the TES were fixed and a bias current scan was performed increasing I_{bias} from zero up to the point of the superconducting transition. The values obtained are then fitted to the Ginzburg-Landau dependence:

$$I_c(T) = I_{c0} * (1 - T/T_c)^{3/2} \quad (4)$$

	<p>WP6 Detectors</p> <p>WP6.2. X-ray sensors</p> <p>WP6.2b Mo/Au pixels</p>	<p>Doc. no.: CSIC AHEAD Report WP6.2b-test</p> <p>Issue : draft 1.0</p> <p>Date : 14/05/2018</p> <p>Page : 11 of 36</p>
		

The good agreement of the fit points to a regime far from Weak Link effects [RD2], as expected from the sizes of the tested devices. Critical current values on the order of those shown in Fig.6 have been obtained for all the measured TES.

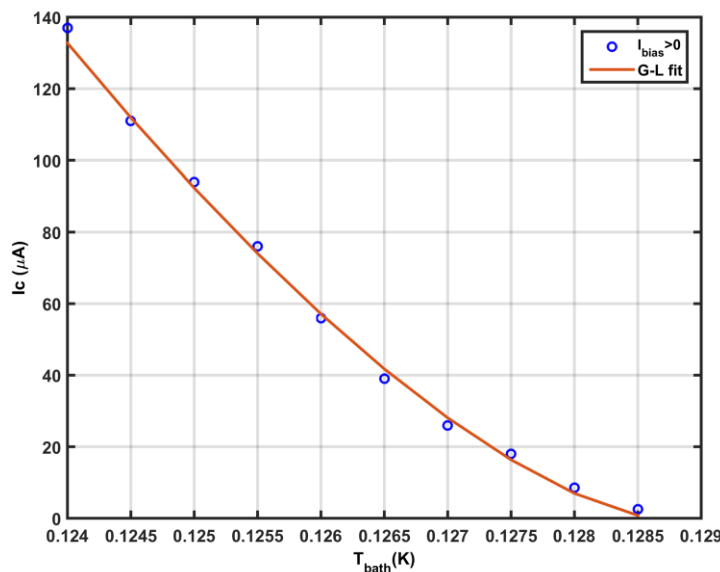


Figure 6. Critical currents of a device, representative of all measured ones. The red line is a fit to Eq.(4)

3.3. Complex impedance

In order to obtain the dynamic parameters of the TESs, namely, logarithmic sensitivity to temperature (α) and to current (β), effective time constant τ_{eff} and heat capacity (C), we perform complex impedance measurements. The set-up is sketched in Fig 7. We use a spectrum analyser HP3265A which provides both a signal source and transfer function measure capabilities. The signal is fed to the TES through a Magnicon I-box (see scheme) which transforms the voltage excitation signal into a current signal and adds it to the DC I_{bias} component. We use a sine wave excitation with small amplitude in order to stay in the linear regime. For a fixed operating point (fixed bath temperature and DC bias current) we perform a frequency sweep from 10Hz to 100KHz (maximum achievable frequency of the apparatus). We configure the instrument to acquire transfer function (Nyquist diagram) with the excitation voltage fed to Ch1 and the output voltage V_{out} fed to Ch2. The transfer function is then read into a PC via GPIB. This process is repeated for several bath temperatures and several percentages of R_n at each temperature. The acquisition at each I_{bias} has been automatized, but the change in bath temperature is still done manually. This is being also automatized which should allow for an increase in the number of operating points characterized.

	<p>WP6 Detectors</p>	<p>Doc. no.: CSIC AHEAD Report WP6.2b-test Issue : draft 1.0 Date : 14/05/2018 Page : 12 of 36</p>
	<p>WP6.2. X-ray sensors WP6.2b Mo/Au pixels</p>	

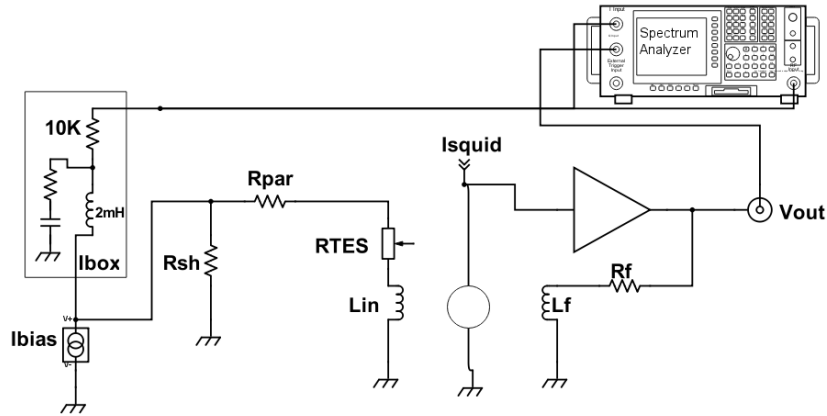


Figure 7. Electrical scheme of the $Z(\omega)$ and noise measurement setup.

From the measured transfer functions ($TF_{meas} = V_{out}/V_{source}$) we can derive the complex impedance of the TES (Z_{TES}). It is customary to use the transfer function in superconducting state (TF_S) in order to cancel out the contribution of the circuit components. Indeed, after some calculations, we can express the measured TF as:

$$TF_{meas} = R_f \left(\frac{M_{in}}{M_f} \right) TF_{out}(\omega) TF_{ibox}(\omega) \frac{R_{shunt}}{Z_{TES} + R_{shunt} + R_{par} + i\omega L} \quad (5.1)$$

where $TF_{out}(\omega)$ is the transfer function of all the components not considered in the scheme and $TF_{ibox}(\omega)$ is the transfer function of the I_{ibox} , which can be approximated in our frequency range for a $10k\Omega$ resistance. In this equation L includes not only the input coil inductance L_{in} but also any parasitic inductance in the circuit. TF_{out} and L are not known but can be estimated from TF measured in normal (TF_N) and superconducting (TF_S) states, where the Z_{TES} is known ($Z_{TES}=0$ in superconducting state and $Z_{TES}=R_n$ in normal state). In this way, again after some calculation, we have:

$$Z_{TES} = \left(\frac{TF_S}{TF_{meas}} - 1 \right) (R_{shunt} + R_{par} + i\omega L) \quad (5.2)$$

In (5.2), everything is now known, since L is estimated from:

$$\frac{TF_S}{TF_N} = \frac{R_n + R_{shunt} + R_{par} + i\omega L}{R_{shunt} + R_{par} + i\omega L} \quad (5.3)$$

In particular, the imaginary part of this expression reaches a minimum which depends on L and by fitting this, we obtained a value of $L=77$ nH. This was done for the first TES and since

	<p>WP6 Detectors</p> <p>WP6.2. X-ray sensors</p> <p>WP6.2b Mo/Au pixels</p>	<p>Doc. no.: CSIC AHEAD Report WP6.2b-test</p> <p>Issue : draft 1.0</p> <p>Date : 14/05/2018</p> <p>Page : 13 of 36</p>
		

the set-up has not changed, it is fixed at this value for all the TESs. Fig 8 reproduces the data and fit for the imaginary part of TF_S/TF_N of ZTES13 from which the value of L was obtained.

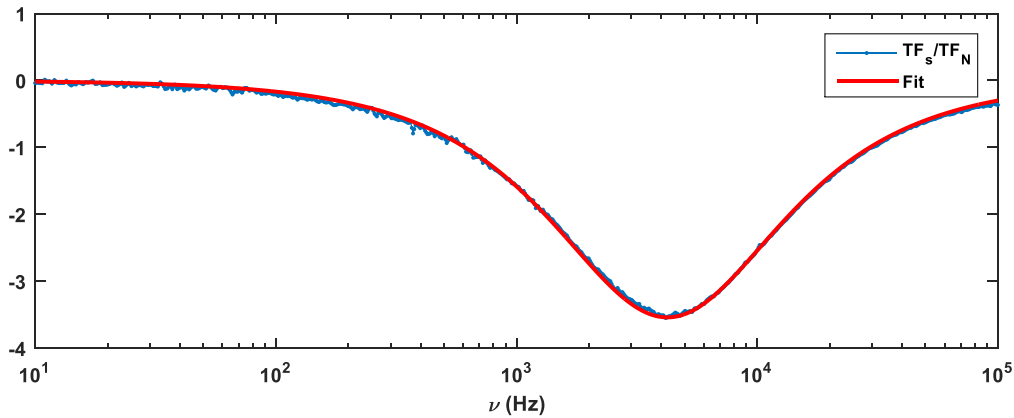


Figure 8. Data and fit of the imaginary part of TFS/TFN for ZTES13 which give $L=77nH$.

Once the $Z_{TES}(\omega)$ are obtained through the above procedure, they are fitted to a theoretical model in order to extract the dynamic parameters. Since we started developing TESs without absorber, the first model considered was the simplest one, the so called single thermal block (STB) model, with a single heat capacity C and a single thermal conductance G . In this case, only two differential equations (1 thermal and 1 electrical) have to be solved. This is done assuming small signal, which allows to linearize the $R(T,I)$ surface of the TES around the operating point resistance R_0 . Under these assumptions, and following [RD1] or [RD6], we arrive at the following expression for the expected TES impedance:

$$Z_{TES} = Z_{inf} + \frac{Z_{inf} - Z_0}{-1 + i\omega\tau_{eff}} \quad (5.4)$$

where

$$Z_{inf} = R_0(\beta + 1) \quad (5.5a)$$

$$Z_0 = R_0(1 + \beta + L_0)/(1 - L_0) \quad (5.5b)$$

$$\tau_{eff} = \tau_0/(L_0 - 1) \quad (5.5c)$$

$$L_0 = P_0\alpha/GT_0 \quad (5.5d)$$

$$\tau_0 = C/G \quad (5.5e)$$

$$\alpha = \left. \frac{\partial \log R}{\partial \log T} \right|_{I_{cte}}, \quad \beta = \left. \frac{\partial \log R}{\partial \log I} \right|_{T_{cte}} \quad (5.5f)$$

Although some of the TESs characterized contain an absorber, only for the last 1Z10 the heat capacity of the absorber was high enough compared to the bilayer capacity. For this reason, the STB model has been used for all the TESs in the fits. Figure 9 shows some $Z_{TES}(\omega)$ in the

	<p>WP6 Detectors</p> <p>WP6.2. X-ray sensors</p> <p>WP6.2b Mo/Au pixels</p>	<p>Doc. no.: CSIC AHEAD Report WP6.2b-test</p> <p>Issue : draft 1.0</p> <p>Date : 14/05/2018</p> <p>Page : 14 of 36</p>
		

imaginary-real plane for several bath temperatures and operating points for two different TESs. In most cases the STB model provides a very good description of the data, as shown on Fig.9 *left*; nevertheless, we display for completeness on Fig.9 *right* an example where this is not the case. This will be discussed in more detail in Section 4.

The fits provide a direct estimate of Z_0 , Z_{inf} and τ_{eff} from which we obtain the parameters we are interested in:

$$\beta = Z_{inf}/R_0 - 1 \quad (5.6a)$$

$$L_0 = (Z_0 - Z_{inf}) / (Z_0 + R_0) \quad \rightarrow \quad \alpha = L_0 G T_0 / P_0 \quad (5.6b)$$

$$\tau_0 = (L_0 - 1) * \tau_{eff} \quad \rightarrow \quad C = G * \tau_0 \quad (5.6c)$$

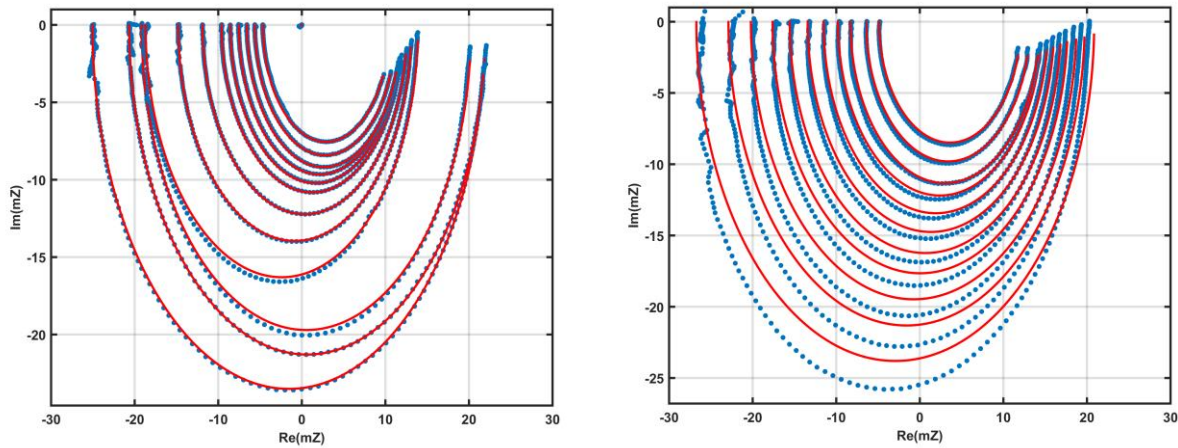


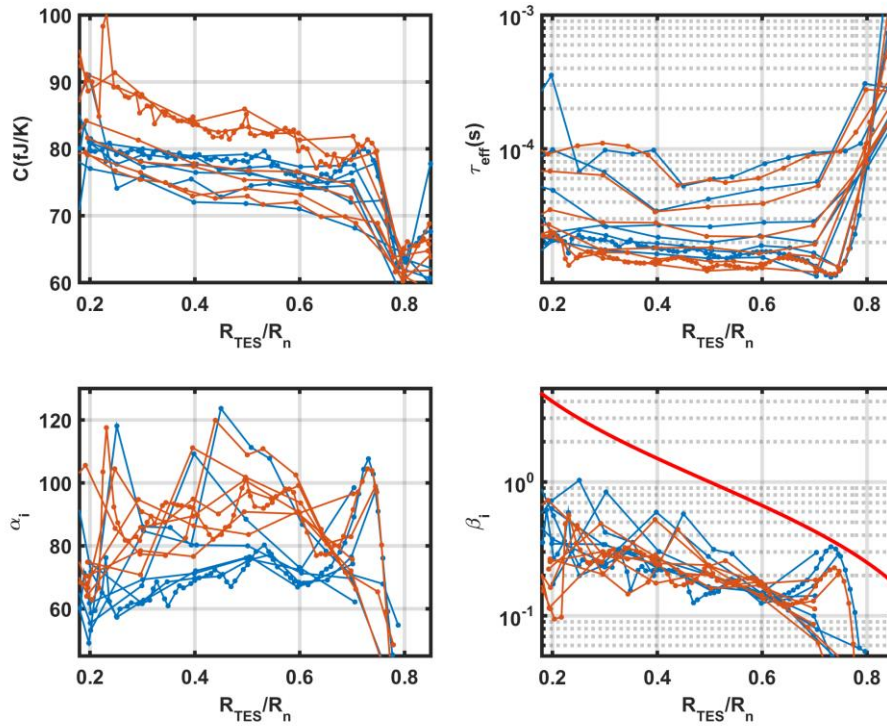
Figure 9. $Z(\omega)$ data for two different TESs at 50mK under positive bias. Red lines are fits to the STB model.

Fig. 10 shows the derived parameters for a typical TES. Again, for robustness, the complex impedance measurements are performed both for positive and negative bias. The results are shown in blue (positive) and orange (negative). Although they are consistent for τ_{eff} and β data, there are more differences for α and C . This seems reasonable, since τ_{eff} is obtained directly from the fit and β depends only on Z_0 , while C and α estimates depend also on L_0 (and therefore Z_0) and G , which we already mentioned that includes its own systematic error of the order of 10%.

Besides the estimate with both polarities, different approaches to the fits have been tested. Real and Imaginary parts of $Z(\omega)$ can be fitted separately or simultaneously. Also the effect of error estimates in Z_0 and Z_{inf} can be propagated to the error estimate in α and β . The results indicate that high in the transition, the most sensitive parameter is β while low in the transition (which is the interesting region to operate the TESs) it is α which is more sensitive to error estimates in Z_0 and Z_{inf} . In any case, the impact of the fit in the systematic error may amount

	<p>WP6 Detectors</p> <p>WP6.2. X-ray sensors</p> <p>WP6.2b Mo/Au pixels</p>	<p>Doc. no.: CSIC AHEAD Report WP6.2b-test</p> <p>Issue : draft 1.0</p> <p>Date : 14/05/2018</p> <p>Page : 15 of 36</p>
		

up to a few percent, but when combined with the uncertainty also in the determination of G leads to errors in α and C that can reach up to 20%. Nonetheless, this does not prevent from getting a coherent and relevant picture of trends for our TESs when doing a combined analysis. In the case of TESs with absorber, another source of error must be the simplification of considering a STB model, as we discuss in Section 4.



Figures 10. Parameters α , β , C and τ_{eff} extracted from complex impedance data for TES 1Z1_23A with positive (blue) and negative (orange) biases and different T_{bath} . The solid line in the β graph corresponds to the so-called two- fluid limit [RD2].

Alpha from IVs

Finally, we would like to comment on another method to validate the estimates of both α and β : it is possible to extract them from the IV curves, which explore also the $R(T,I)$ surface but in different directions (neither I_{TES} nor T_{TES} are constant during a IV curve, only T_{bath} is). Simple calculations allow converting from one representation to the other. In our case we decide to define an effective alpha as the logarithmic sensitivity of $R(T,I)$ with respect to TES temperature but along an IV direction. This α_{eff} can be expressed as a function of the α and β obtained from the $Z(\omega)$ measurements. Similarly we can define an effective beta as a

	<p>WP6 Detectors</p> <p>WP6.2. X-ray sensors</p> <p>WP6.2b Mo/Au pixels</p>	<p>Doc. no.: CSIC AHEAD Report WP6.2b-test</p> <p>Issue : draft 1.0</p> <p>Date : 14/05/2018</p> <p>Page : 16 of 36</p>
		

logarithmic sensitivity with respect current in the IV direction. We have the following relationships:

$$\alpha_{eff} = \frac{\alpha (2L_0 + \beta)}{(2 + \beta)L_0} \quad (6.1)$$

$$\beta_{eff} = \frac{\beta + 2L_0}{1 - L_0} \quad (6.2)$$

Fig. 11 shows a comparison of these effective parameters obtained directly from the IVs or from the $Z(\omega)$ of a typical TES. Both methods are completely independent so the agreement is again an indication of the robustness of the measurements. For some cases and for low $\%R_n$ there are some differences in α , which could be sign of some systematic error in the estimates. More detailed analyses are needed in order to understand the origin of those differences. Note also the divergence in β_{eff} which comes from the presence of $(1-L_0)$ in the denominator of eq. (6b) and the fact that L_0 becomes 1 high in the transition for this TES.

Unless otherwise specified, the α values reported in sections 4 and 5 correspond to those extracted from the complex impedance.

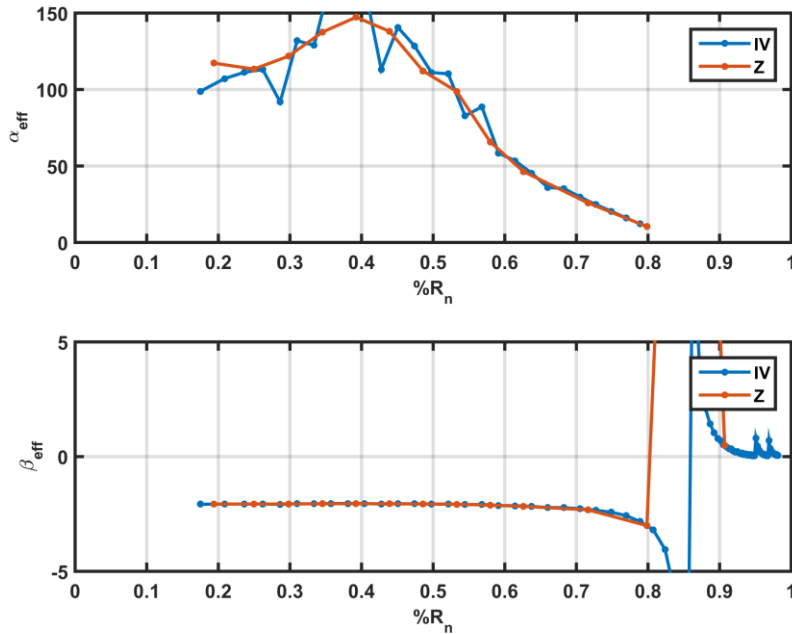
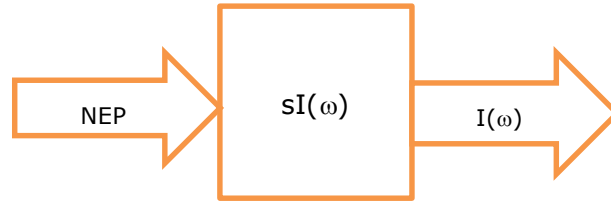


Figure 11. Comparison of the effective α and β (see text for definition) as obtained from IV curves or $Z(\omega)$ data for a typical TES.

	WP6 Detectors WP6.2. X-ray sensors <i>WP6.2b Mo/Au pixels</i>	Doc. no.: CSIC AHEAD Report WP6.2b-test Issue : draft 1.0 Date : 14/05/2018 Page : 17 of 36
		

3.4 Noise measurements

The same set-up described in Fig. 7 for the complex impedance measurements is used to obtain also noise spectra. Actually, for each operating point, the acquisition protocol measures both the transfer function and the noise. The experimental data obtained from the analyzer is in units of Volt/Hz^{0.5} which is then converted into TES current noise (in a similar way as the V_{out} is converted into I_{TES} in the IV measurements). The HP is configured to average a few samples and the frequency range is set from 10Hz to 100KHz. These noise spectra already in pA/Hz^{0.5} are compared to the theoretical noise model. This model is built from the STB model and makes use of the dynamic parameters extracted from the $Z(\omega)$ measurement at that same operating point. The noise components considered are as in [RD1]: phonon noise and Johnson noise in the TES, Johnson noise in the shunt resistance, and a constant noise term from the SQUID, which are added in quadrature. An important element in the model is the power to current responsivity $s_I(\omega)$ which allows to express the current noise at the output into a noise equivalent power (NEP) at the input, which is also a relevant information. Conversely this responsivity allows converting a power level at the TES into a current response. The expressions involved are the following:



$$i_{TES}(\omega) \left[\frac{A}{Hz^{0.5}} \right] = NEP(\omega) \left[\frac{W}{Hz^{0.5}} \right] * |s_I(\omega)| \left[\frac{A}{W} \right] \quad (7)$$

$$s_I(\omega) = \frac{-1}{i_0 R_0} \left(\frac{L}{\tau_{el} R_0 L_0} + \left(1 - \frac{R_L}{R_0} \right) + i\omega \frac{L\tau}{R_0 L_0} \left(\frac{1}{\tau_I} + \frac{1}{\tau_{el}} \right) - \frac{\omega^2 L\tau}{R_0 L_0} \right)^{-1} \quad (8)$$

- Phonon: $i_{TFN}^2(\omega) = 4K_b T_0^2 G |s_I(\omega)|^2 F(T_0, T_{bath})$
- Johnson: $i_{TES}^2(\omega) = 4K_b T_0 I_0^2 R_0 (1 + 2\beta_I) (1 + \omega^2 \tau_0^2) |s_I(\omega)|^2 / L_0^2$
- Shunt: $i_{Rsh}^2(\omega) = 4K_b T_{bath} I_0^2 R_L (L_0 - 1)^2 (1 + \omega^2 \tau_0^2 / (L_0 - 1)^2) |s_I(\omega)|^2 / L_0^2$
- SQUID: $i_{SQUID}(\omega) = 3pA / Hz^{0.5}$

$$i_{total}^2(\omega) = i_{TFN}^2(\omega) + i_{TES}^2(\omega) + i_{sh}^2(\omega) + i_{SQUID}^2(\omega)$$



WP6 Detectors

WP6.2. X-ray sensors

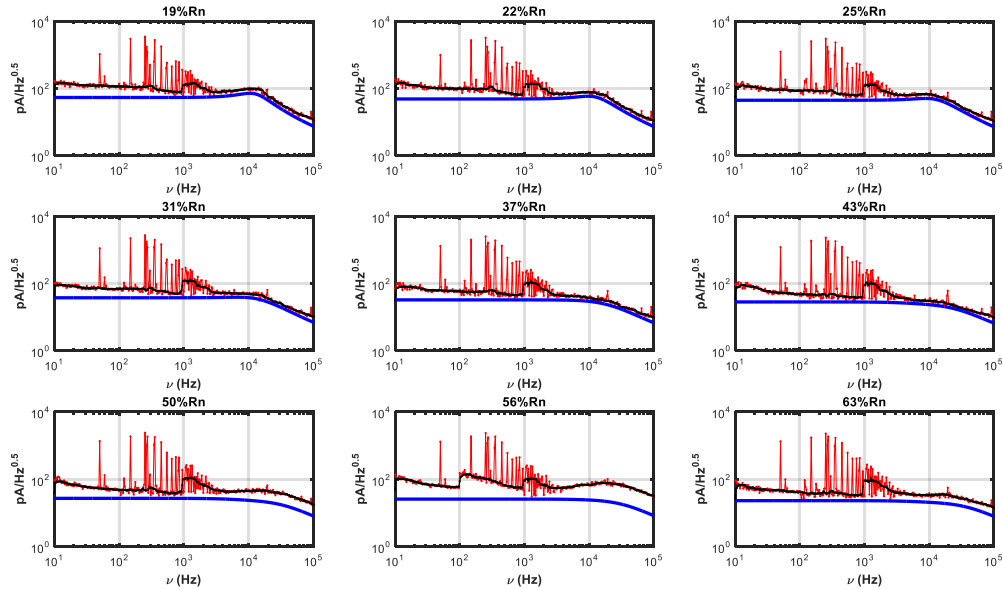
WP6.2b Mo/Au pixels

Doc. no.: CSIC AHEAD Report WP6.2b-test

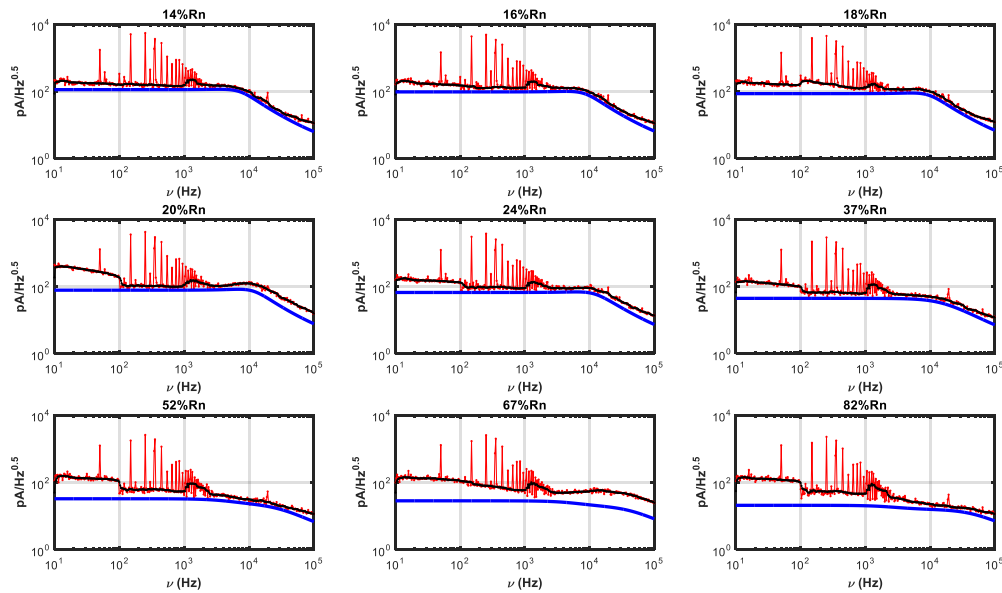
Issue : draft 1.0

Date : 14/05/2018

Page : 18 of 36



Figs.12a Current noise spectra recorded at different biases and 50mK for device 1Z1_54A. In red the experimental data, in black the smoothed spectra and in blue the calculated spectra using the simplest model and the experimental TES parameters.



Figs.12b Current noise spectra recorded at different biases and 70mK for device 1Z1_54A. Colors and lines have the same meaning as in Fig.12a.

	<p>WP6 Detectors</p>	<p>Doc. no.: CSIC AHEAD Report WP6.2b-test Issue : draft 1.0 Date : 14/05/2018 Page : 19 of 36</p>
	<p>WP6.2. X-ray sensors <i>WP6.2b Mo/Au pixels</i></p>	

Fig. 12 shows current spectra at 50 mK (a) and 70 mK (b) for one of the devices at various operating points. In red the experimental data, in black smoothed data and in blue the noise spectra calculated using the experimental TES parameters and the simplest model [RD1]. Some aspects are worth mentioning. Even if the set-up is not optimized for noise measurements, the noise levels are not far from those expected for these TESs. Of course, quite a few resonance peaks are visible in the data which will worsen parameters as the derived baseline spectral resolution. These seem not intrinsic to the TESs and should be reduced in further optimizations of the set-up. In the meantime, we can filter these features via software (black lines). Some artifacts are also visible; the most remarkable is a jump in some spectra in the first decade. This appears to be a problem of the HP analyzer which is preventing us for the moment to perform detailed analysis at very low frequencies. Very rarely this is also observed in other decades.

The actual difference between the measured spectra and the model is usually named Excess Noise and is described in literature as a factor M which parametrizes this difference. The definition of M is as follows:

$$i_{exp}^2(\omega) = i_{th}^2(\omega) * (1 + M^2) \quad (9a)$$

$$M^2 = \frac{i_{exp}^2 - i_{th}^2}{i_{th}^2} \quad (9b)$$

It simply represents the contribution of an excess unknown noise component as a fraction with respect to the expected theoretical value:

$$i_{excess}(\omega) = i_{th}(\omega) * M \quad (9c)$$

This could be applied to the overall experimental noise, but in practice, there can be different excess components, so it is customary to define excess terms for different components [RD4, RD5]. The most widely used in literature is an excess component with the same dependence as the Johnson noise and is therefore termed $M_{johnson}$. This component accounts for the unexplained noise at high frequencies. Since we observe also a discrepancy at low frequencies, we have defined also a phonon-like excess term, which we call M_{phonon} and should account for the unexplained noise at low frequencies. Fig. 13 displays two spectra at 50 mK and two operating points for a typical TES. The STB model and the result from adding the excess M terms are also shown.

It should be noted that these M terms are simply a means to quantify our ignorance about the actual noise model, but are useful parameters in order to compare the noise performance of different TESs and different operating points. These terms may become unnecessary if new noise contributions are added to the model. In particular, for models with more than one thermal block, new noise terms emerge as the internal thermal fluctuation noise (ITFN) between the blocks. These ITFN terms may behave as phonon or Johnson noise depending on

	<p>WP6 Detectors</p> <p>WP6.2. X-ray sensors</p> <p>WP6.2b Mo/Au pixels</p>	<p>Doc. no.: CSIC AHEAD Report WP6.2b-test</p> <p>Issue : draft 1.0</p> <p>Date : 14/05/2018</p> <p>Page : 20 of 36</p>
		

the topology. As discussed in the complex impedance section, it is not clear which blocks can be reasonably added in our bare TESs, but for the case of TESs with absorber made of Au, this constitutes a natural new block which should lead to an ITFN term and in principle, to a more accurate noise prediction.

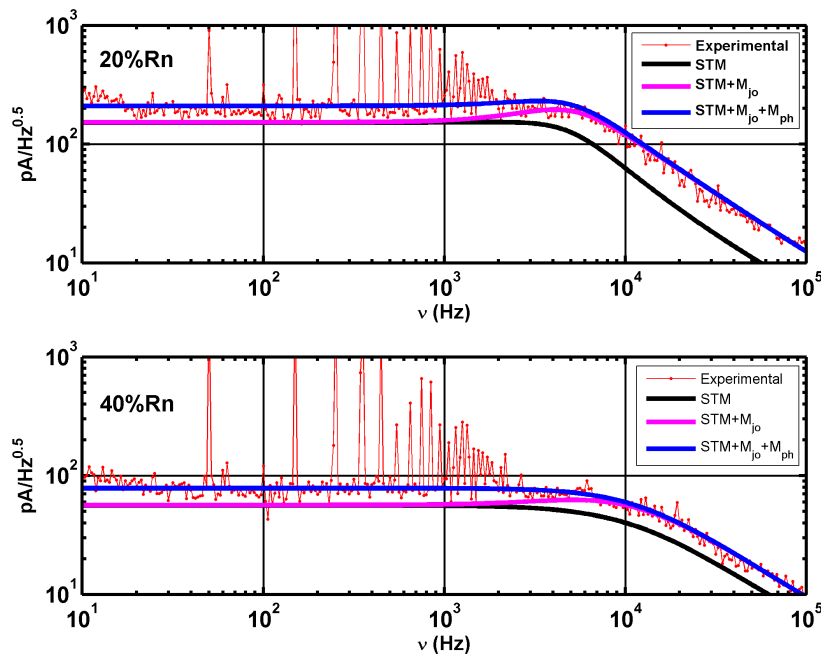


Figure 13. Noise spectra recorded at 50mK for 20%R_n and 40%R_n for one of the devices. The three lines are the models described in the text.

As mentioned at the beginning of this section, the NEP is also relevant to characterize the TESs. For devices working in integration mode, it is a direct measure of the minimum detectable input power. In our case it can be used to compute the minimum energy resolution that can be achieved under optimal conditions. We call this limit baseline resolution and it is measured in electronvolts (eV). The expression to use is:

$$\Delta E_{fwhm} = \frac{2\sqrt{2\log(2)}}{\sqrt{\int_0^{\infty} \frac{4}{NEP(\omega)^2} d\omega}} \quad (10)$$

Fig. 14 shows two NEP at 50mK and two different operating points. In red the experimental spectrum, in black a smoothed spectrum and in blue the STB model with the dynamic parameters extracted from the $Z(\omega)$ measurements. Fig. 15 displays the calculated baseline resolution for that TES at all recorded bath temperatures and along the transition. As it can be seen, below 60% of R_n the behaviour is quite flat and close to 1eV and even below for the lowest bath temperatures.



WP6 Detectors

WP6.2. X-ray sensors
WP6.2b Mo/Au pixels

Doc. no.: CSIC AHEAD Report WP6.2b-test
Issue : draft 1.0
Date : 14/05/2018
Page : 21 of 36

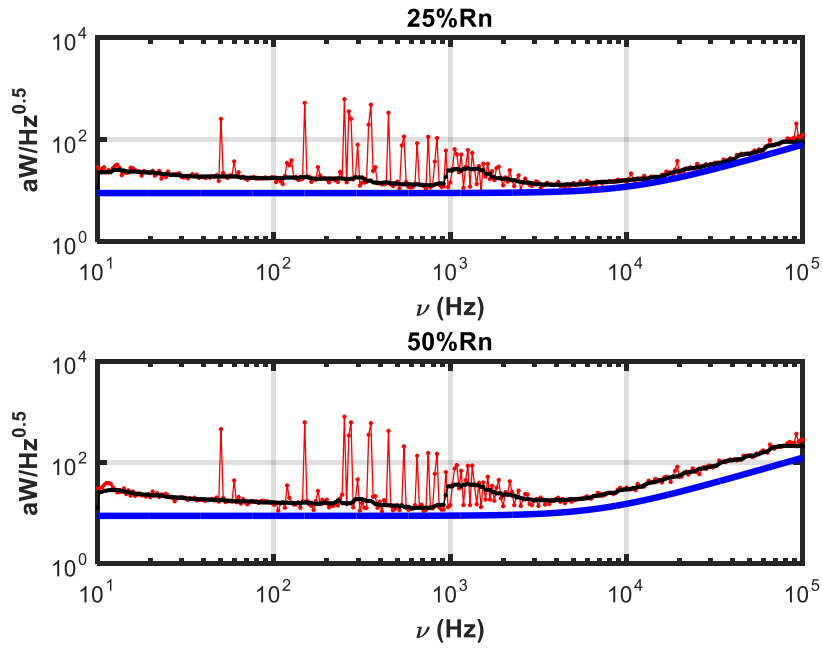


Figure 14. NEP at 50 mK for a typical TES at 25% and 50% of R_n . Experimental (red), smoothed (black) and STB model (blue).

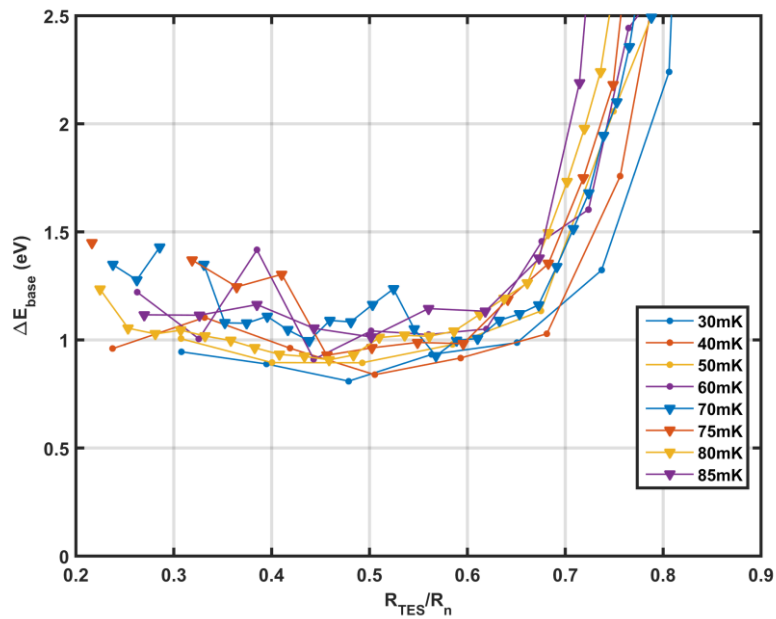


Figure 15. Baseline spectral resolution at different T_{bath} , for the same TES as data in Fig. 14.

	<p>WP6 Detectors</p> <p>WP6.2. X-ray sensors</p> <p><i>WP6.2b Mo/Au pixels</i></p>	<p>Doc. no.: CSIC AHEAD Report WP6.2b-test</p> <p>Issue : draft 1.0</p> <p>Date : 14/05/2018</p> <p>Page : 22 of 36</p>
		

4. Analysis of results

In this section, we analyse the values and behaviour of the parameters for the tested devices. It must be taken into account that the aim of this WP is to mature the Mo/Au TES technology, and for that it is essential first to assess whether the fabricated devices display a reproducible, robust and expected behaviour; next, it is important to identify their standard response, i.e. their performances and the evolution of them with basic parameters of operation and design, since this will allow identification of the route for further improvement. Hence, most of the section corresponds to the analysis of the main TES parameters as a function of bias and T_{bath} (section 4.1.). After, in section 4.2. the effect of banks is discussed. Tables 3 and 4 below summarize the main parameters for all of them.

It should be noted that both the analysis and acquisition software and protocols have evolved from the first measured devices. This has resulted in a somehow heterogeneous set of data with the first devices having a much smaller set of operating points and information in them, in particular noise spectra and all the information derived from them. For the first devices we also suffered the limitation of a current source which did not allow putting the TES into normal state at low temperatures (maximum current $500\mu\text{A}$). This meant that we had to use an external source and the process of acquiring IV curves was totally manual. With the incorporation of a new current source this could be automatized.

Design A	ZTES13	ZTES18	ZTES20	ZTES25	ZTES26	ZTES28
$R_{\text{para}} (\mu\Omega)$	120	66	66	45	55	75
$R_N (\text{m}\Omega)$	14.9	12.5	8.9	15	13.5	16
n	3.1-3.3	3.1-3.3	3.0-3.2	3.25-3.35	3.4	3.42
$G (\text{pW/K})$	300-320	130-140	75-95	330-350	390	410
$T_c (\text{mK})$	115	91	90	110	109	113
$C (\text{fJ/K})$	300-370	65-85	30-50	150-200	100	110
α	90-100	50-70	40-85	200	50-100	100
β	0.12-0.20	0.25-0.35	0.18-0.35	0.15-0.4	1-0.01	1-0.01
$\tau_{\text{eff}} (\mu\text{s})$	50-400	40-140	40-160	10-1000	10-	10-
M_{Johnson}	-	1.5	-	0.6-4	0.7	0.6-1.6
M_{phonon}	-	0.8	-	0.8	0.6	0.6
$\Delta E_{\text{baseline}} (\text{eV})$	-	0.9	-	1.2-2	1.0	0.9

Table 3. Parameters of tested devices with Design A, extracted from dark characterization. The values correspond to any T_{bath} far from T_c and to the lower $\%R_N$ achieved for each device.

	WP6 Detectors WP6.2. X-ray sensors <i>WP6.2b Mo/Au pixels</i>	Doc. no.: CSIC AHEAD Report WP6.2b-test Issue : draft 1.0 Date : 14/05/2018 Page : 23 of 36
		

Design B	1Z1_54A	1Z1_23A	1Z1_54B	1Z2_35A	1Z10_45B
R_{para} ($\mu\Omega$)	28	20	50	48.56	260
R_N ($m\Omega$)	29	23	29	26.7	11.8
n	3.3	3.4	3.2	3.03	3.05
G (pW/K)	260	260	235	310	90
T_c (mK)	98	97	103	129	91.5
C (fJ/K)	40-60	70-80	95	450	200
α	100	60-70	100-200	100-200	50-100
β	1	0.2	1-2	1-2	1
τ_{eff} (μs)	10	20	10	50	180
$M_{johnson}$	0.5-0.8	0.8	0.5-1.5	2.5	1.5-4
M_{phonon}	0.8-1.0	0.6	0.7-1.4	0.9	1-2
$\Delta E_{baseline}$ (eV)	0.7	0.8	1.0	2.7	1.8-4.5

Table 4. Parameters of tested devices with Design B, extracted from dark characterization. The values correspond to any T_{bath} far from T_c and to the lower $\%R_n$ achieved for each device. Ranges or values at high $\%R_n$ are used when the devices present instabilities or anomalous data.

4.1 Evolution of main TES parameters as a function of bias and T_{bath}

Thermal Conductance G

The thermal conductances G of all the characterized TES are summarized in Fig 16a. Differences arise both from the TES geometries and membrane thickness and from the different T_c for each TES. In order to cancel out the effect of the different T_c , we have normalized G at 100mK. The result, G_{100} , is shown in Fig 16b against the radiative area, namely, the TES perimeter times the membrane thickness. Data are well described by a linear fit, as expected for the case of thermal conduction dominated by radiation. As discussed in section 3, a systematic error on the order of 10% has to be considered, which accounts for most of the deviations from the linear dependence.

From these results, it follows that G values close to LPA2 specifications for the X-IFU instrument of Athena (115pW/K) can be achieved with our TES of T_c of 100 mK using TES areas close $100 \times 100 \mu m^2$ (design B with membrane thickness $0.5 \mu m$); decreasing T_c to 90 mK would give even more flexibility to achieve the required G .

Regarding the thermal conduction exponent n , for all TES it is nearly constant for most $\% R_n$, taking values between 3 and 3.5, as expected (Fig. 16c).



WP6 Detectors

WP6.2. X-ray sensors
WP6.2b Mo/Au pixels

Doc. no.: CSIC AHEAD Report WP6.2b-test
Issue : draft 1.0
Date : 14/05/2018
Page : 24 of 36

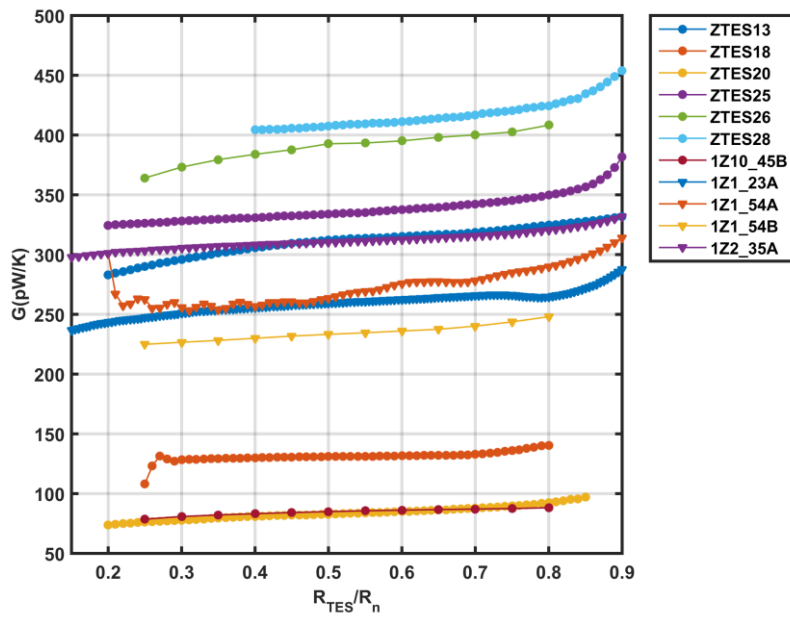


Figure 16a. Thermal conductance along the transition as derived from P-T fits.

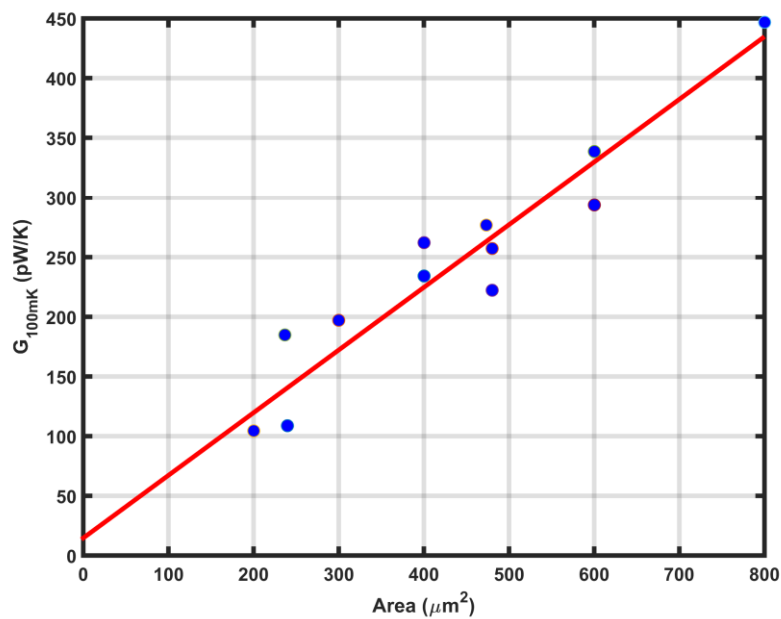


Figure 16b. Thermal conductance normalized at 100mK as a function of the radiative area (TES perimeter times membrane thickness); the red line is a fit to the expected linear dependence.

	<p>WP6 Detectors</p> <p>WP6.2. X-ray sensors</p> <p>WP6.2b Mo/Au pixels</p>	<p>Doc. no.: CSIC AHEAD Report WP6.2b-test</p> <p>Issue : draft 1.0</p> <p>Date : 14/05/2018</p> <p>Page : 25 of 36</p>
		

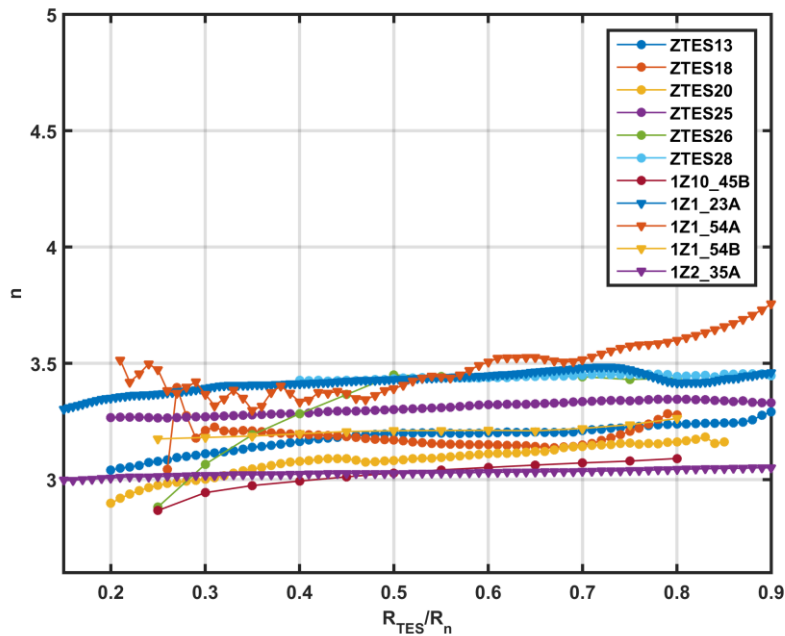


Figure16c. Thermal exponent n extracted from P - T fits.

Heat Capacity

As shown in the graphs of C as a function of the operation point (Figs. 17), most of the devices have heat capacities consistent with the volume of the TES bilayer: C along the transition falls between the estimated C values for the bilayer in the normal state and the maximal value for the C jump in the superconducting transition expected from the BCS theory. It must be considered that the significant thickness of the bilayer implies that the heat capacity of bare TES is considerably high, in fact becoming dominant even when Bi absorbers are present, because of the much smaller heat capacity of Bi and the relatively small area of the absorbers fabricated in this WP. There are three devices displaying higher C values: the heat capacity of TES 1Z10_45B, the only one with Au absorber, can be accounted for by the contribution of the latter and is indicative that LPA2 specifications would be met incorporating in the absorber electroplated Au slightly thinner than the $1.4 \mu\text{m}$ in this TES, if absorber area is $240 \mu\text{m}^2$. ZTES13 and 1Z2_35A display C values too high, which could be partially attributed to their quite higher T_c ; even more, these two devices are respectively the first tested (fabrication process not optimized) and the first in which membrane opening was performed at the end of the fabrication process; indeed, in some chips of this batch Si remains were observed because of inhomogeneous attack. Both factors could account for the unexpectedly high C values.



WP6 Detectors

WP6.2. X-ray sensors
WP6.2b Mo/Au pixels

Doc. no.: CSIC AHEAD Report WP6.2b-test
Issue : draft 1.0
Date : 14/05/2018
Page : 26 of 36

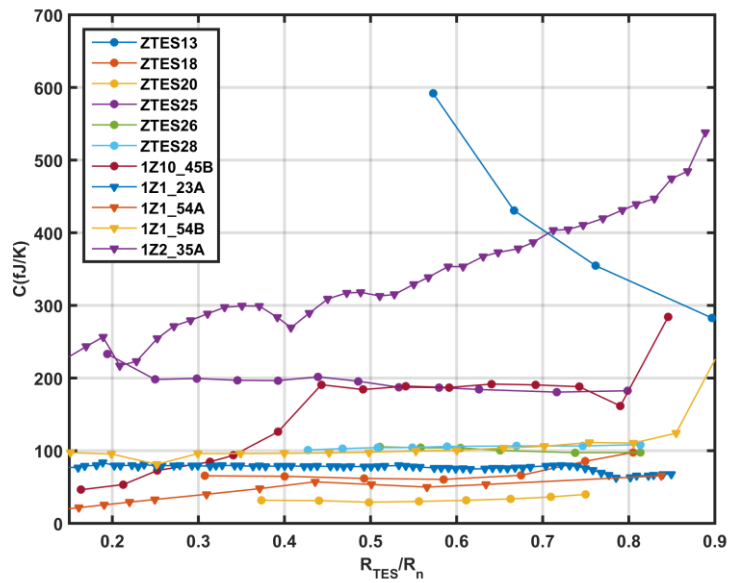


Figure 17a. Heat capacity obtained at 50 mK, as a function of bias.

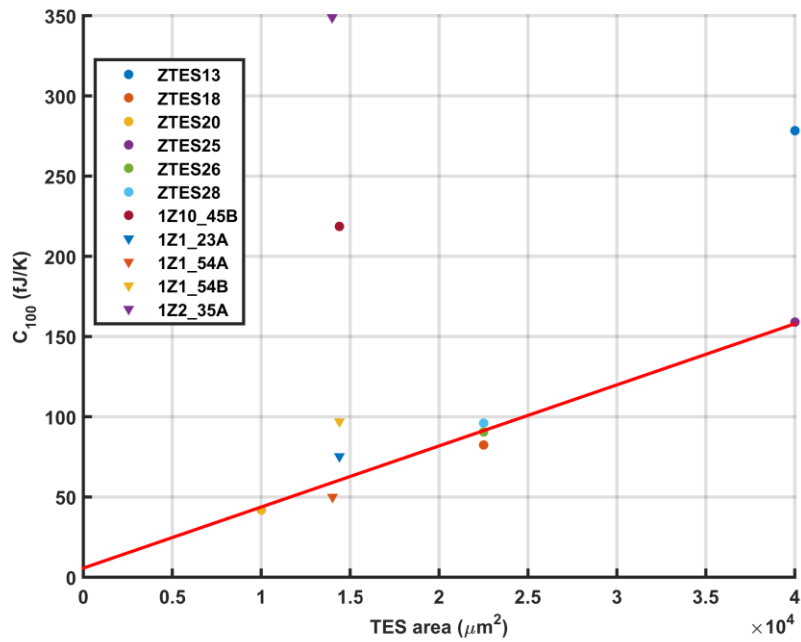


Figure 17b. Heat capacity obtained at 50mK, as a function of TES (Mo/Au) area.

	<p>WP6 Detectors</p> <p>WP6.2. X-ray sensors</p> <p>WP6.2b Mo/Au pixels</p>	<p>Doc. no.: CSIC AHEAD Report WP6.2b-test</p> <p>Issue : draft 1.0</p> <p>Date : 14/05/2018</p> <p>Page : 27 of 36</p>
		

Dynamic parameters (α , β , τ_{eff})

Fig. 18a shows the α values as a function of T_{bath} , for constant bias; it can be seen that for the bath temperatures of interest α is nearly constant. Fig. 18b allows comparison of α values at 50 mK as a function of the bias point, for the tested devices. Values range from 50 to 100 at low $\%R_n$. Nonetheless, since we have been using an R_{shunt} of 2 m Ω , we have been able to characterize our devices only over that resistance value. This, and also some instabilities in the faster TES, have prevented characterization of the TES below $\%R_n \sim 20-35\%$, typically the most favourable region to operate TES. In the case of β , values and behaviour are also close to commonly reported; as shown in Fig. 19 β values fall in the region of the so called two-fluid regime, indicating no effect from weak link, as expected from the dimensions of all tested TESs. No clear conclusions can be driven from the α and β values as a function of TES size and design, pointing to the fact that the transition shape is mainly governed by other effects.

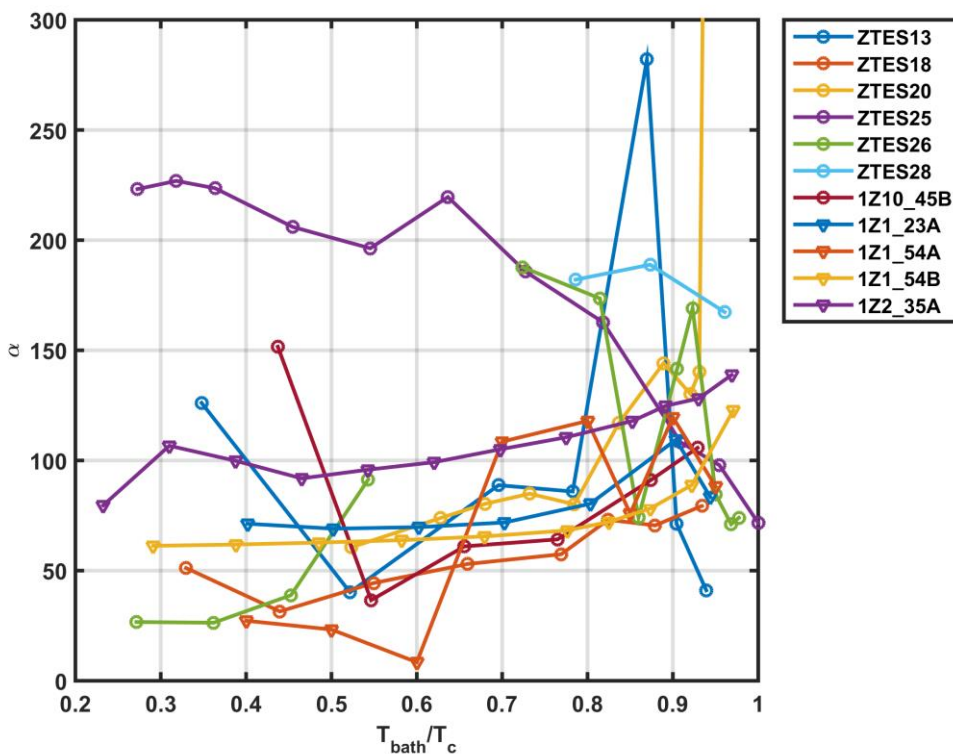


Figure 18a. α at 40% R_n versus the reduced temperature T_{bath}/T_c .



WP6 Detectors

WP6.2. X-ray sensors
WP6.2b Mo/Au pixels

Doc. no.: CSIC AHEAD Report WP6.2b-test
Issue : draft 1.0
Date : 14/05/2018
Page : 28 of 36

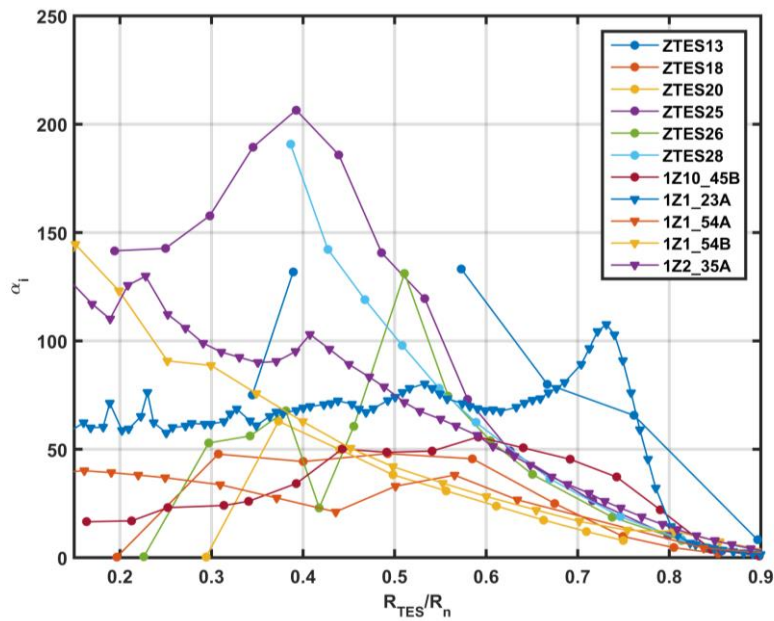


Figure 18b. α at 50 mK, as a function of bias.

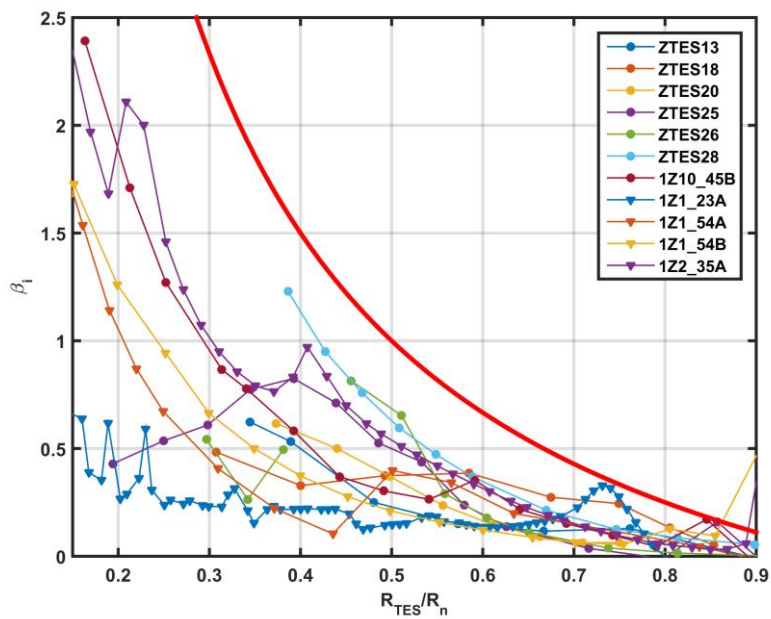


Figure 19. β as a function of bias at 50mK. The red line delimits the area where the two-fluid model is expected to hold [RD2].



WP6 Detectors

WP6.2. X-ray sensors
WP6.2b Mo/Au pixels

Doc. no.: CSIC AHEAD Report WP6.2b-test
Issue : draft 1.0
Date : 14/05/2018
Page : 29 of 36

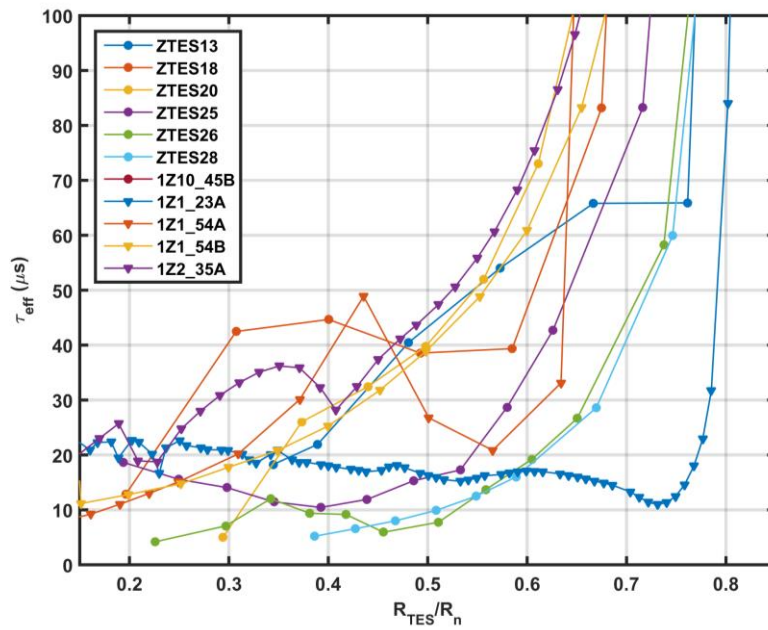
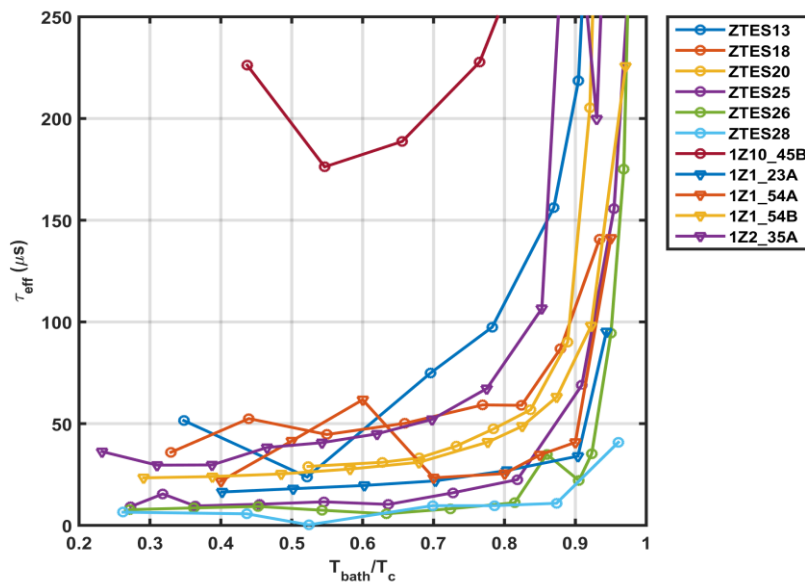


Figure 20a. Effective time constant at $T_{\text{bath}} = 50 \text{ mK}$.



Figs. 20b. Effective time constant at 40% R_n as a function of the reduced temperature T_{bath}/T_c .

	<p>WP6 Detectors</p> <p>WP6.2. X-ray sensors</p> <p><i>WP6.2b Mo/Au pixels</i></p>	<p>Doc. no.: CSIC AHEAD Report WP6.2b-test</p> <p>Issue : draft 1.0</p> <p>Date : 14/05/2018</p> <p>Page : 30 of 36</p>
		

Figs. 20 display the effective time constants for all devices as a function of bias point and bath temperature; below 80% of T_c τ_{eff} is quite flat and therefore insensitive to bath temperature. Also, τ_{eff} is quite independent of the bias point, in the region of interest.

For most tested devices, τ_{eff} values are of a few tens of microseconds, as expected from their low heat capacity. Device 1Z10_45A, with higher C due to the presence of the electroplated Au absorber, has $\tau_{\text{eff}} \sim 200 \mu\text{s}$, on the order of LPA2 requirements. As discussed before, this evidences that the required time constants would be reached when using absorbers of the required area ($240 \mu\text{m}$) and slightly thinner electroplated Au.

Excess Noise and Baseline Resolution

As described in section 3, noise spectra are compared to a noise model based on a single thermal block (STB). We do not fit the spectra, but use the dynamic parameters obtained from the complex impedance fits to produce an expected noise spectrum using this model [RD1]. The difference between measured and expected spectra, the excess noise, is described by means of the M factors described in section 3. A few aspects are worth taking in view. On one hand, excess noise refers to contributions not accounted for by the noise model. Since we are dealing with the simplest model, it is expected that non zero values are obtained if we are neglecting some noise term. For the case of bare TESs without absorber, it is not clear which extra terms should be contributing, although the results from our G fits may point to a contribution from the membrane in some cases. Electron-phonon decoupling could produce also an additional contribution. When the devices include absorber, this is a clear block to add to the model, and we expect to reduce the values of M by including them, which doesn't actually mean reducing the excess noise, but just the amount of 'unexplained' noise. In the very last term, it is the experimental energy resolution that will give a measure of the actual TES performance. In the lack of it, these M factors (for a given model) and also the baseline energy calculated from NEP allow for a comparison of different TES designs or to assess the impact of noise mitigation strategies in the sensors or in the set-up.

Regarding the excess noise contributions (Figs.21), it is found that the extra Johnson component lies below 2 for most TESs and biases. No clear dependence on any TES parameter has been observed at this stage. The last TES characterized, 1Z10_45B, the one with the highest heat capacity, seems to have also the highest excess noise, below 50% R_n . This may be intrinsic to the TES, but it has also coincided with the need to change the characterization SQUID and the presence of some unusual noise in the set-up. Indeed, also the excess phonon noise component for this TES is higher. We plan to characterize more TES with absorbers (notably for devices with $240 \mu\text{m}$ absorbers) in a new modified and improved set-up in order to better understand whether this is a true worsening of the noise or it is just instrumental. Nonetheless, further understanding of noise and characterization of TES performances will definitely come with the detection of pulses and measurement of spectral resolution, scheduled for the near future.



WP6 Detectors

WP6.2. X-ray sensors

WP6.2b Mo/Au pixels

Doc. no.: CSIC AHEAD Report WP6.2b-test

Issue : draft 1.0

Date : 14/05/2018

Page : 31 of 36

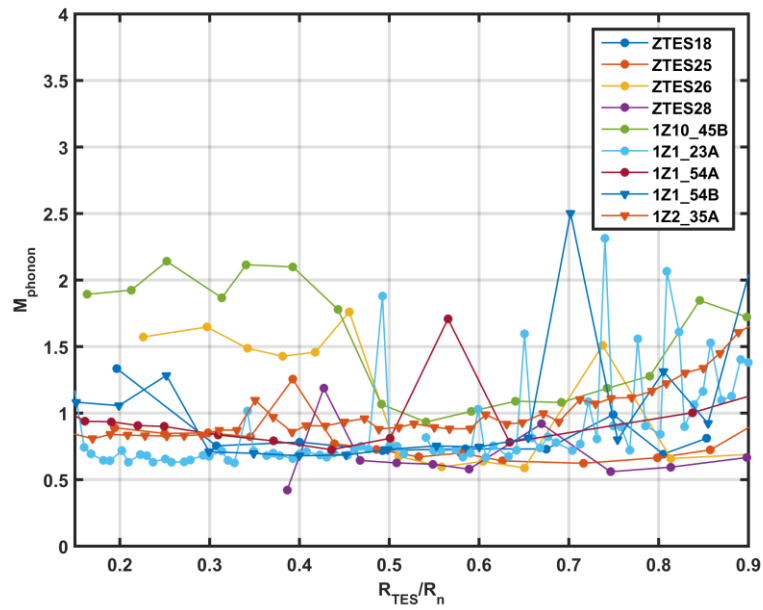
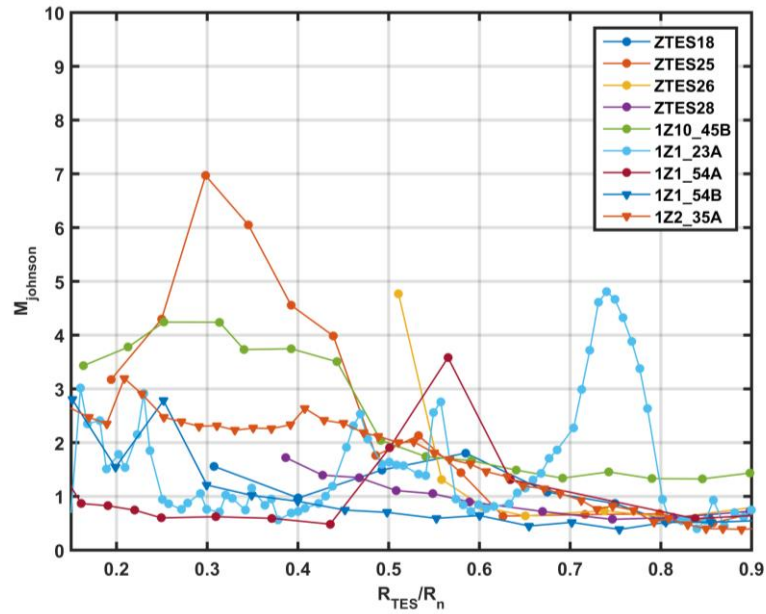


Figure 21. Excess noise parameters at 50 mK, M_{johnson} (top) and M_{photon} (bottom), as described in section 3.4.

	<p>WP6 Detectors</p> <p>WP6.2. X-ray sensors</p> <p>WP6.2b Mo/Au pixels</p>	<p>Doc. no.: CSIC AHEAD Report WP6.2b-test</p> <p>Issue : draft 1.0</p> <p>Date : 14/05/2018</p> <p>Page : 32 of 36</p>
		

The extra phonon noise contribution displays values between 0.7 and 1 for all devices and appears to be not correlated to any TES parameter, nor to the presence of the absorber (at least when this is Bi; in the case of Au the fact that only one device has been tested does not allow this conclusion); its origin is not clear, and could be associated to the setup. On one hand, as it has been mentioned, the introduction of more sophisticated models should help improving the estimate at least for those TES with absorber, where an internal thermal fluctuation noise is expected. On the other hand, we have observed that this excess term is correlated with the F factor in the phonon noise term: as it is well known, for two blocks in thermal equilibrium there exists a phonon noise term associated with thermal fluctuations between them, i.e the usual phonon noise; when one of the blocks is colder, the total noise is lower and this is taken into account by the $F(T_0, T_{\text{bath}})$ term in the equation for the phonon noise (see section 3). We have observed that we can very well reproduce the experimental noise by forcing $F=1$, which is the case when T_{bath} equals T_c . This may point to the presence of an internal thermal fluctuation noise between two blocks at T_c , as for example an electron-phonon decoupling in the bilayer, or to the effect of vibrations or other thermal external noise that acts on the TES and spoils the benefit of operating at low bath temperatures. We plan further analysis to understand this issue.

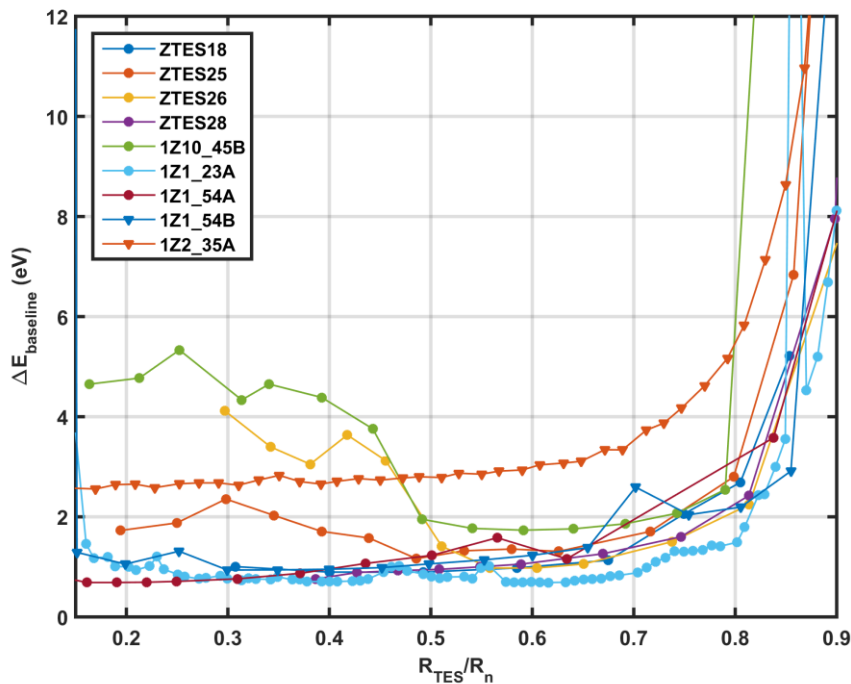


Figure 22. Experimental baseline spectral resolution obtained from the NEP, at $T_{\text{bath}}=50\text{mK}$.

	<p>WP6 Detectors</p>	<p>Doc. no.: CSIC AHEAD Report WP6.2b-test Issue : draft 1.0 Date : 14/05/2018 Page : 33 of 36</p>
	<p>WP6.2. X-ray sensors <i>WP6.2b Mo/Au pixels</i></p>	

Fig.22. shows the baseline spectral resolution, obtained from the experimental NEP spectra. At low biases it is quite independent of bias and also of T_{bath} . The values are promisingly small for most devices, although this is of course a lower limit to the true spectral resolution achievable with an X-ray source. TESs with higher $\Delta E_{\text{baseline}}$ are the already discussed 1Z10_45B (Au absorber), 1Z2_35A (with anomalously high C) and ZTES26 (note that points of ZTES26 under 50% R_n are not reliable because it was unstable in that region (see next section)). On the contrary, the best $\Delta E_{\text{baseline}}$ corresponds to devices 1Z1_54A, 1Z1_23A and 1Z1_54B; this might be correlated to TES design B and to the improvement of the TES fabrication procedure and should be confirmed in the near future. No clear relationship is found between α and $\Delta E_{\text{baseline}}$.

4.2 Effect of banks

As discussed in [AD1], banks were initially included in the first TES design (A); later on, improvements in fabrication procedure allowed fabrication of devices with excellent transitions without the need of banks. We present here a comparison of main TES performances for 2 identical TESs, with and without banks: ZTES26 and ZTES28, respectively. Both were processed individually; even more, ZTES28 was the first tested device without banks.

The resistive transitions of both devices are remarkably similar, in spite of being shifted 4 mK (see Fig.3 in [AD1]). Figs. 23 to 25 depict α , the baseline energy resolution and M factors for both TES. Again, results are remarkably close; from them, we concluded that banks were not required in these devices, and where not added in the TES fabricated afterwards.

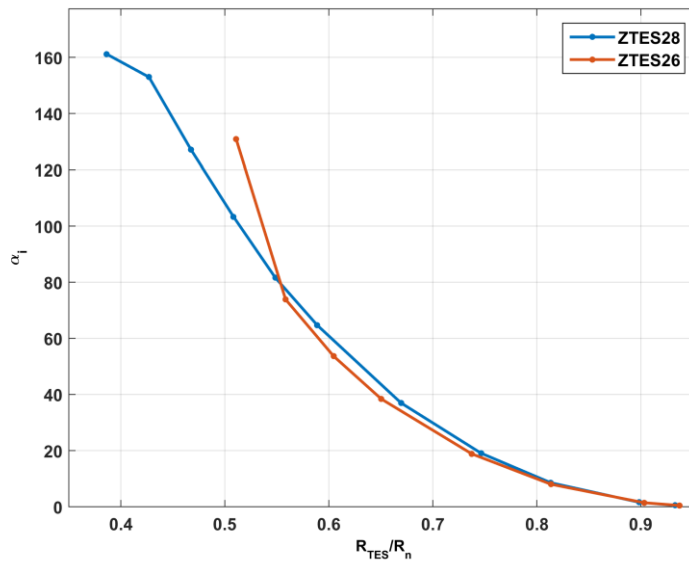


Figure 23. Comparison of α parameter along the transition at 50mK for ZTES26 and ZTES28.

	<p>WP6 Detectors</p> <p>WP6.2. X-ray sensors</p> <p>WP6.2b Mo/Au pixels</p>	<p>Doc. no.: CSIC AHEAD Report WP6.2b-test</p> <p>Issue : draft 1.0</p> <p>Date : 14/05/2018</p> <p>Page : 34 of 36</p>
		

We should point out that these two TES have higher G and therefore are faster devices. This resulted in an instability of the circuit below 50% R_n as can be inferred from the noise spectra. The complex impedance also reflects this instability. For this reason, we could not characterize them at lower $\%R_n$.

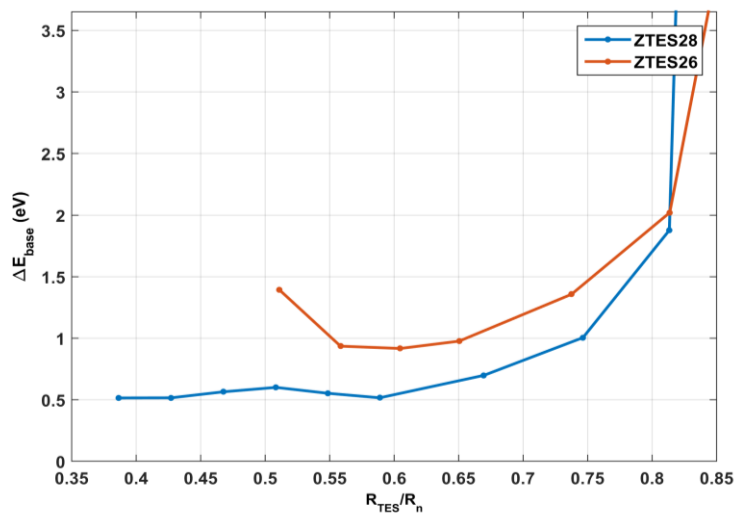


Figure 24. Baseline spectral resolution at 50 mK for ZTES26 and ZTES28.

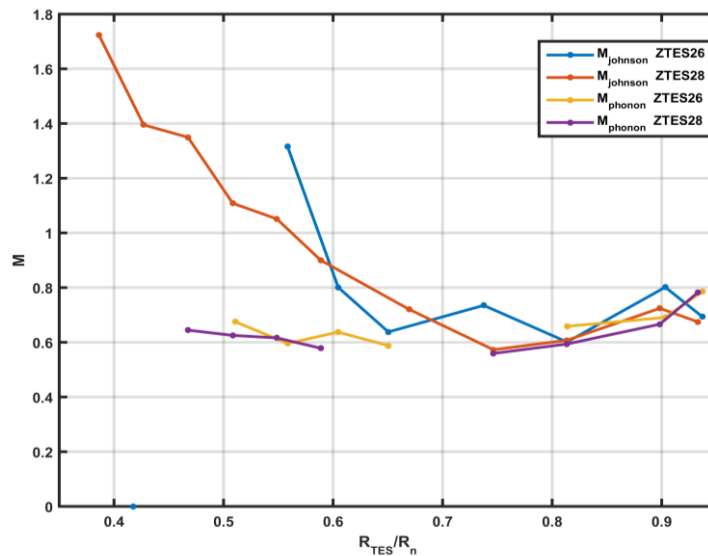


Figure 25. Excess noise factors at 50 mK for ZTES26 and ZTES28.

	<p>WP6 Detectors</p> <p>WP6.2. X-ray sensors</p> <p><i>WP6.2b Mo/Au pixels</i></p>	<p>Doc. no.: CSIC AHEAD Report WP6.2b-test</p> <p>Issue : draft 1.0</p> <p>Date : 14/05/2018</p> <p>Page : 35 of 36</p>
		

5. CONCLUSIONS

Full dark characterization of 11 Mo/Au TES devices, without and with absorbers, with different designs and sizes, has been performed. The devices fabricated and tested display:

- Consistent and mostly expected overall behaviour.
- α values between 50 and 100 at low biases, as most state of the art TESs
- Rather low excess noise (without using normal metal structures)
- Very promising baseline spectral resolution
- Tunable G with slight changes of TES area
- R_n in the range 10-40 m Ω , tunable by changing bilayer geometry, adding banks, or changing the d_{Mo}/d_{Au} thickness, as shown in [AD1].

Most devices had no absorber or a central Bi absorber (typical size 100 μm); because of this, the heat capacity contribution of the absorber was not dominant, and the effective time constants were excessively small. The last measured device was the only one with Au absorber (although of area still too small); it displayed an increase of the heat capacity as expected, and therefore also larger effective time constant. The systematic and coherent behaviour of the devices tested allows for an extrapolation of the measured parameters, in order to provide an estimate of the baseline pixel that would meet basic X-IFU LPA2 requirements: a suitable G can be achieved with devices as those measured, with membrane thickness 0.5 μm and TES size $\sim 100 \mu\text{m}$, while required time constants would be easily reached when using absorbers of the required LPA2 area (240 μm) by lowering slightly the electroplated Au thickness. We have also shown [AD1] that other relevant basic TES parameters, such as T_c and R_n , can be tuned (and in fact are already calibrated) within the suitable operating ranges in order to readjust TES performances.

Of course, the actual performances of these devices and its improvement, together with a better understanding of noise, will come with the test of devices with large area absorbers and with the capability of measuring spectral resolution; which, even though not included in the present WP6 planning, are scheduled for the near future.

6. FUTURE WORK

CSIC will continue development of Mo/Au TESs. The lines of work in the immediate future are:

- Test of more devices with designed parameters closer to X-IFU specifications. Particularly, Bi/Au absorbers of larger area.
- Further improvements in the set-up, to be able to (i) perform a more efficient characterization of device in terms of time (capability of measuring more devices per cooling down), (ii) reach lower % R_n , and (iii) improve noise.
- Improvement of the thermal models and noise models, to better understand the intrinsic noise of the devices.

	<p>WP6 Detectors</p>	<p>Doc. no.: CSIC AHEAD Report WP6.2b-test</p>
	<p>WP6.2. X-ray sensors</p> <p><i>WP6.2b Mo/Au pixels</i></p>	<p>Issue : draft 1.0</p> <p>Date : 14/05/2018</p> <p>Page : 36 of 36</p>

- Studies of the underlying TES physics (origin of the transition, weak link, phase slip effects...)
- Detection of pulses and measurement of experimental spectral resolution.

	TES Detector Development for Athena / X-IFU	
CTP 2015 – WP4 Optimization of a European Transition Edge Sensor Array	TECHNICAL NOTE 2.6	Doc. no.: SRON-XIFU-TN-2015-063 Issue : 1.0 Date : 15-03-2018 Page : 2 of 12

Document Change Record

Issue	Date	Changed Section	Description of Change
1.0	15-03-2018	All	Initial draft

	TES Detector Development for Athena / X-IFU	 <small>ATHENA X-ray Integral Field Unit</small>
CTP 2015 – WP4 Optimization of a European Transition Edge Sensor Array	TECHNICAL NOTE 2.6	Doc. no.: SRON-XIFU-TN-2015-063 Issue : 1.0 Date : 15-03-2018 Page : 3 of 12

Abbreviations and acronyms	4
Applicable Documents	4
Reference Documents	4
1 TES design aspects	5
1.1 TES size	5
1.2 Si support structure and SiN membrane	5
1.3 Metallic bars for alpha tuning	5
1.4 TES resistance	5
1.5 Critical current	6
1.6 Summary of the expected parameters	6
1.7 Au and Au/Bi absorbers	7
2 Short description of TES chips on a single wafer	8
2.1 Chips 1-9:	9
2.2 Chips R1-R6:	9
2.3 Chips R7-R8:	10
2.4 Chips R9-R10:	11
2.5 Chips R11-R12:.....	12

	TES Detector Development for Athena / X-IFU	
CTP 2015 – WP4 Optimization of a European Transition Edge Sensor Array	TECHNICAL NOTE 2.6	Doc. no.: SRON-XIFU-TN-2015-063 Issue : 1.0 Date : 15-03-2018 Page : 4 of 12

Abbreviations and acronyms

Item	Meaning
TES	Transition Edge Sensor
GSFC	Goddard Space Flight Center
X-IFU	X-ray Integral Field Unit
FDM	Frequency Division Multiplexing
Tc	Critical temperature
Rn	Normal state resistance

Applicable Documents

[AD#]	Doc. Reference	Issue	Title
[AD1]			

Reference Documents

[RD#]	Doc. Reference	Issue	Title
[RD1]	Appl. Phys. Lett. 111, 192602 (2017);		Eliminating the non-Gaussian spectral response of X-ray absorbers for transition-edge sensors
[RD2]	ESA-CTP Technical Note 9.5a		Mask Design for 1k-pixel functional arrays
[RD3]			
[RD4]			
[RD5]			
[RD6]			
[RD7]			
[RD8]			
[RD9]			

	TES Detector Development for Athena / X-IFU	
CTP 2015 – WP4 Optimization of a European Transition Edge Sensor Array	TECHNICAL NOTE 2.6	Doc. no.: SRON-XIFU-TN-2015-063 Issue : 1.0 Date : 15-03-2018 Page : 5 of 12

1 TES design aspects

In the course of this study, it became clear that more iteration on device fabrication and tests are needed in order to arrive at the optimum design. However, from what we have learned so far by testing both SRON and GSFC devices, we are confident that the next batch of devices is a major step forward toward a TES array that meets the X-IFU requirements.

1.1 TES size

The current TES size is too large ($100 \times 140 \mu\text{m}^2$) and experience with GSFC devices shows that it is more likely to achieve better energy resolution with smaller size TESes, where IV curves are smoother and have less structures. Since the heat conductance (G) is proportional to the perimeter of the TES, smaller devices will be slower and help us get closer to the desired speed. It is also encouraging that our best results so far are from low- G devices so lowering the G further might lower the over all noise as well.

1.2 Si support structure and SiN membrane

Our devices so far only have vertical Si bars and the next fabrication runs will have Si grid support structure that is needed for large arrays. This is likely to increase the G to some extent (less that factor of 2), which can be compensated by reducing the membrane thickness. The SiN thickness is currently $1 \mu\text{m}$ and can be safely reduced to $0.5 \mu\text{m}$. As we know from experience with bolometer TESes, reducing the heat capacity of the thermal link between the TES and the bath reduces the thermal fluctuation noise. Therefore, thinning the SiN is likely to reduce the noise too. If the TESes become too slow, we can have the full membrane with no slots.

1.3 Metallic bars for alpha tuning

Our conclusion so far is that presence of the metallic bars on the TES is essential for reducing alpha and avoiding pulse saturation. Full size absorbers are about a factor of 2.2 larger and will be less prone to pulse saturation. Increasing the heat capacity increases the noise and therefore in the new fabrication run we will reduce the thickness of gold absorbers to $2 \mu\text{m}$ (currently is $3 \mu\text{m}$). The best absorber coupling is with 5 contact points with the one in the center on a metallic bar so far.

Recent GSFC detectors shows that bars are not needed. In spite of having very large alpha, beta and the excess noise, they have achieved remarkable energy resolutions of below 2 eV. We will explore this option in our detectors by simply skipping the metallic bar process step. If this approach is successful, we need to make thicker absorber to make sure device can handle 12 keV without saturation and pay some noise penalty.

1.4 TES resistance

The current TES resistance is above $200 \text{ m}\Omega$ and too high. It is worthwhile to explore the performance of the TESes with lower resistance. The resistance will immediately go down by a factor of 1.4 by choosing a square TES geometry (currently TESes are rectangular $140 \times 100 \mu\text{m}^2$). Tuning the Ti/Au thicknesses in the bilayer can further reduce the resistance. For the next batch, we are aiming at $\text{Ti/Au} = 24/114 \text{ nm}$ that should give $T_c \sim 90 \text{ mK}$ and $R_n \sim 80 \text{ m}\Omega$. This is likely to reduce the noise too since recent GSFC devices with similar resistance have shown energy resolutions well below 3 eV.

	TES Detector Development for Athena / X-IFU	 ATHENA X-ray Integral Field Unit
CTP 2015 – WP4 Optimization of a European Transition Edge Sensor Array	TECHNICAL NOTE 2.6	Doc. no.: SRON-XIFU-TN-2015-063 Issue : 1.0 Date : 15-03-2018 Page : 6 of 12

1.5 Critical current

The T_c of our devices are currently around 100-105 mK, which is higher than the X-IFU requirement (i.e. 90 mK). Tuning the device resistance will be combined with reducing the T_c to 90 mK, which is also reduces the noise.

1.6 Summary of the expected parameters

Taking all the above discussions into account, Table 1 summarizes the parameters for the $80 \times 80 \mu\text{m}^2$ TES as an example. By reducing the size of the TES, the G will go down by a factor of 2.5 to around 100 pW/K. The larger and thinner absorber will increase the C to around 0.8 pJ/K. As it is explain in section 2, we also consider 100×100 and $120 \times 120 \mu\text{m}^2$ TESes for k-pixel arrays.

Table 1. TES parameters for TES-19 (best device so far), TES-goal (expected for next run) and LPA2 (X-IFU requirement) in comparison.

Parameters	TES-19	TES-goal $80 \times 80 \mu\text{m}^2$	LPA2
T_b [K]	0,05	0,05	0,05
T_c [K]	0,1	0,1	0,09
P [pW]	7,5	3	2,7
n	3,5	3,5	3
C [pJ/K]	0,6	0,8	0,8
G [pW/K]	263	105	90
τ [ms]	2,3	7,6	8,9
α	32	75	75
Loop gain	9	21	25
τ_{eff} [μs]	451	724	734
R_n [$\text{m}\Omega$]	250	250	250
R_0 [$\text{m}\Omega$]	50	50	50
E (6keV) [fW]	1	1	1
dT (6keV) [mK]	1,67	1,25	1,25
dR (6keV) [$\text{m}\Omega$]	27	47	52
R_h (6keV pulse) [$\text{m}\Omega$]	77	97	102
R_h (12keV pulse) [$\text{m}\Omega$]	103	144	154

The orange marked values are the inputs and the others are calculated from the given parameters. dR and dT are the resistance and the temperature change when a photon hits the absorber. dT is calculated using the energy of the photon ($E=6$ or 12 keV, which is about 1 or 2 fJ) divided by the heat capacity C . dR is calculated using dT and alpha. R_h is maximum resistance during a pulse assuming a constant alpha in the transition and that is to estimate the pulse saturation. As we see the R_h is below R_n (normal state resistance), which means no pulse saturation expected for 12 keV photons with alpha as high as 75.

	TES Detector Development for Athena / X-IFU	 <small>ATHENA X-ray Integral Field Unit</small>
CTP 2015 – WP4 Optimization of a European Transition Edge Sensor Array	TECHNICAL NOTE 2.6	Doc. no.: SRON-XIFU-TN-2015-063 Issue : 1.0 Date : 15-03-2018 Page : 7 of 12

1.7 Au and Au/Bi absorbers

Our energy resolution measurements on all devices that have Au/Bi full-size absorbers show low energy tails in the spectra, similar to what is shown in Fig. 1. This was not seen in any of the devices with half-size Au absorbers. This behaviour is most likely associated with the quality of Bi that can be estimated by measuring of the RRR [RD1]. Bismuth with RRR close to 1 has a semi-metal behaviour, which is considered good as an absorber. Bismuth with $RRR < 0.5$ has a semiconductor behaviour and can cause such low energy tails in the spectra.

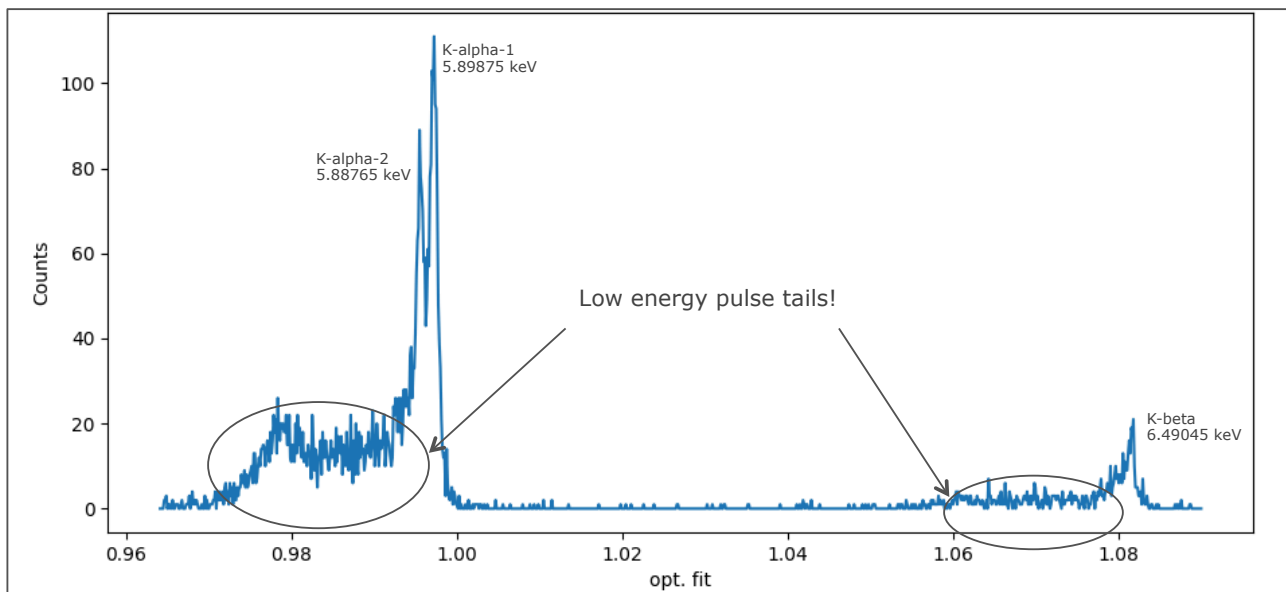


Fig. 1. An example of low energy tails, present in the measured spectra of Fe-55 X-ray source using all our devices with Au/Bi full-size absorbers.

In order to address the Bi problem without hindering the progress on the other aspects, we have decided to follow two parallel routes: In the next fabrication run we only use large Au absorbers. While these devices are being tested, we will try to improve our electroplated Bi quality and once acceptable RRR of the representative layer is achieved, another batch of devices with Au/Bi absorbers will be fabricated.

	TES Detector Development for Athena / X-IFU	 ATHENA X-ray Integral Field Unit
CTP 2015 – WP4 Optimization of a European Transition Edge Sensor Array	TECHNICAL NOTE 2.6	Doc. no.: SRON-XIFU-TN-2015-063 Issue : 1.0 Date : 15-03-2018 Page : 8 of 12

2 Short description of TES chips on a single wafer

There are 21 chips on the next batch as follows (see Fig. 2.). The mask design is already reported in detail elsewhere [RD2]. However, for the sake of completeness of this TN, we chose to repeat some the main features of the detector design.

Chip	TES (μm^2)	Description
1	100 x 100	1000 pixel array; uniform reference design
2	100 x 100	1000 pixel array; uniform reference design, GSFC wiring
3	100 x 100	1000 pixel array; uniform reference design, GSFC wiring
4	80 x 80	1000 pixel array; uniform reference design
5	80 x 80	1000 pixel array; uniform reference design, GSFC wiring
6	80 x 80	1000 pixel array; uniform reference design, GSFC wiring
7	120 x 120	1000 pixel array; uniform reference design
8	120 x 120	1000 pixel array; uniform reference design, GSFC wiring
9	120 x 120	1000 pixel array; uniform reference design, GSFC wiring
R1	100 x 100	Uniform 5x5 array; reference for 1, 2, 3
R2	100 x 100	Uniform 5x5 array; reference for 1, 2, 3
R3	80 x 80	Uniform 5x5 array; reference for 4, 5, 6
R4	80 x 80	Uniform 5x5 array; reference for 4, 5, 6
R5	120 x 120	Uniform 5x5 array; reference for 7, 8, 9
R6	120 x 120	Uniform 5x5 array; reference for 7, 8, 9
R7	Variable	Variable TES & variable slot size
R8	Variable	Variable TES & variable slot size
R9	Variable	Pixel optimization study (noise, absorber coupling) – set 1
R10	Variable	Pixel optimization study (noise, absorber coupling) – set 1
R11	Variable	Pixel optimization study (noise, absorber coupling) – set 2
R12	Variable	Pixel optimization study (noise, absorber coupling) – set 2

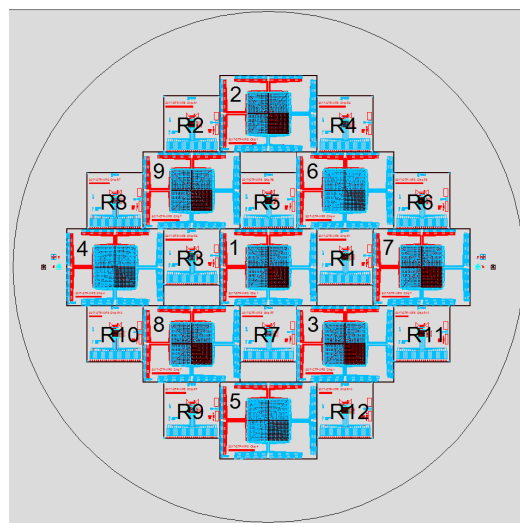
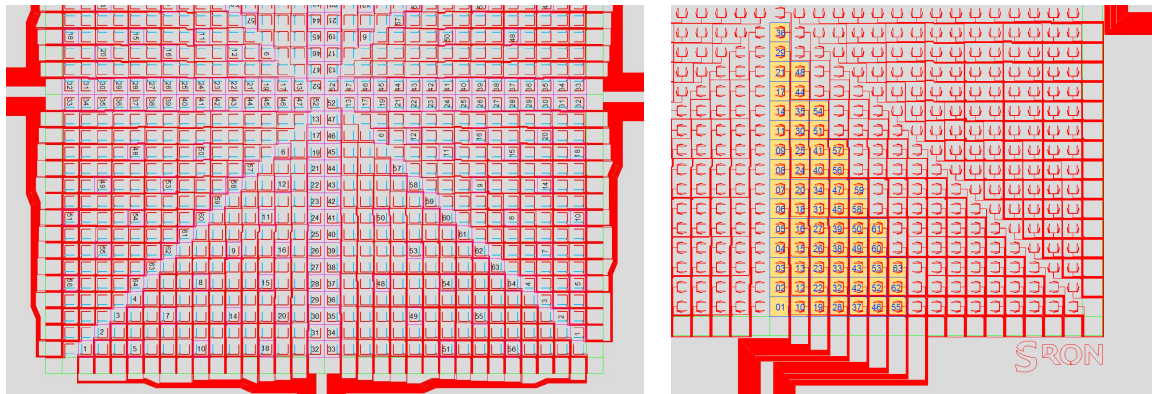


Fig. 2. Overview of chips on a 100 mm diameter wafer

	TES Detector Development for Athena / X-IFU	
CTP 2015 – WP4 Optimization of a European Transition Edge Sensor Array	TECHNICAL NOTE 2.6	Doc. no.: SRON-XIFU-TN-2015-063 Issue : 1.0 Date : 15-03-2018 Page : 9 of 12

2.1 Chips 1-9:

- 9 arrays of 1k-pixel TESes: 32x32 uniform pixels, 4x64 pixels are wired.
- 3 different TES sizes: 80x80, 100x100 and 120x120 μm^2 .
- 2 types of wiring: Original and GSFC like (see Fig. 3.).



Original wiring design:

- 4x64 pixels are wired across the array
- Good for uniformity tests

Goddard like wiring design:

- 4x64 pixels are wired in one corner
- Good for cross talk measurement

Fig. 3. Wiring types of the 1k-pixel arrays.

2.2 Chips R1-R6:

5x5 uniform arrays with exact design as the k-pixel chips , i.e. 80x80, 100x100 and 120x120 μm^2 .

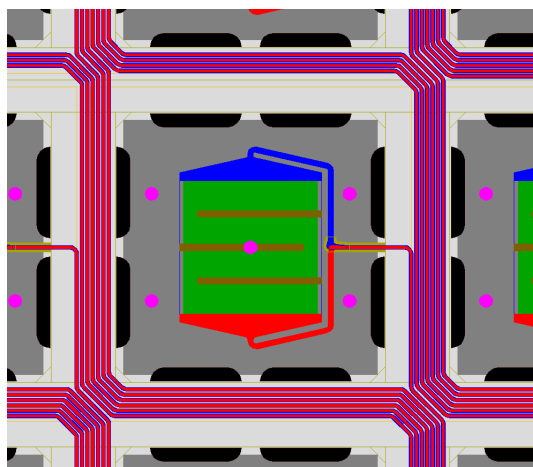


Fig. 3. Preferred pixel design for k-pixel array and reference chips

	TES Detector Development for Athena / X-IFU	 <small>ATHENA X-ray Integral Field Unit</small>
CTP 2015 – WP4 Optimization of a European Transition Edge Sensor Array	TECHNICAL NOTE 2.6	Doc. no.: SRON-XIFU-TN-2015-063 Issue : 1.0 Date : 15-03-2018 Page : 10 of 12

2.3 Chips R7-R8:

These chips are designed to study the dependence of the heat conductivity value G as a function of geometry. From left to right the TES area changes from $120 \times 120 \mu\text{m}^2$ to $50 \times 50 \mu\text{m}^2$. (Sequence: 120, 100, 80, 60, 50).

From bottom to top the size of the slots, etched into the membrane, change such that 15%, 24%, 31%, 67% and 100% of the perimeter is left to conduct the heat. Using the diffuse heat conduction model (section 1.2), the value of G is expected to change from about 40 pW/K to 100 pW/K for the $100 \times 100 \mu\text{m}^2$ TES. For the columns with smaller TES size, the expected G will be lower.

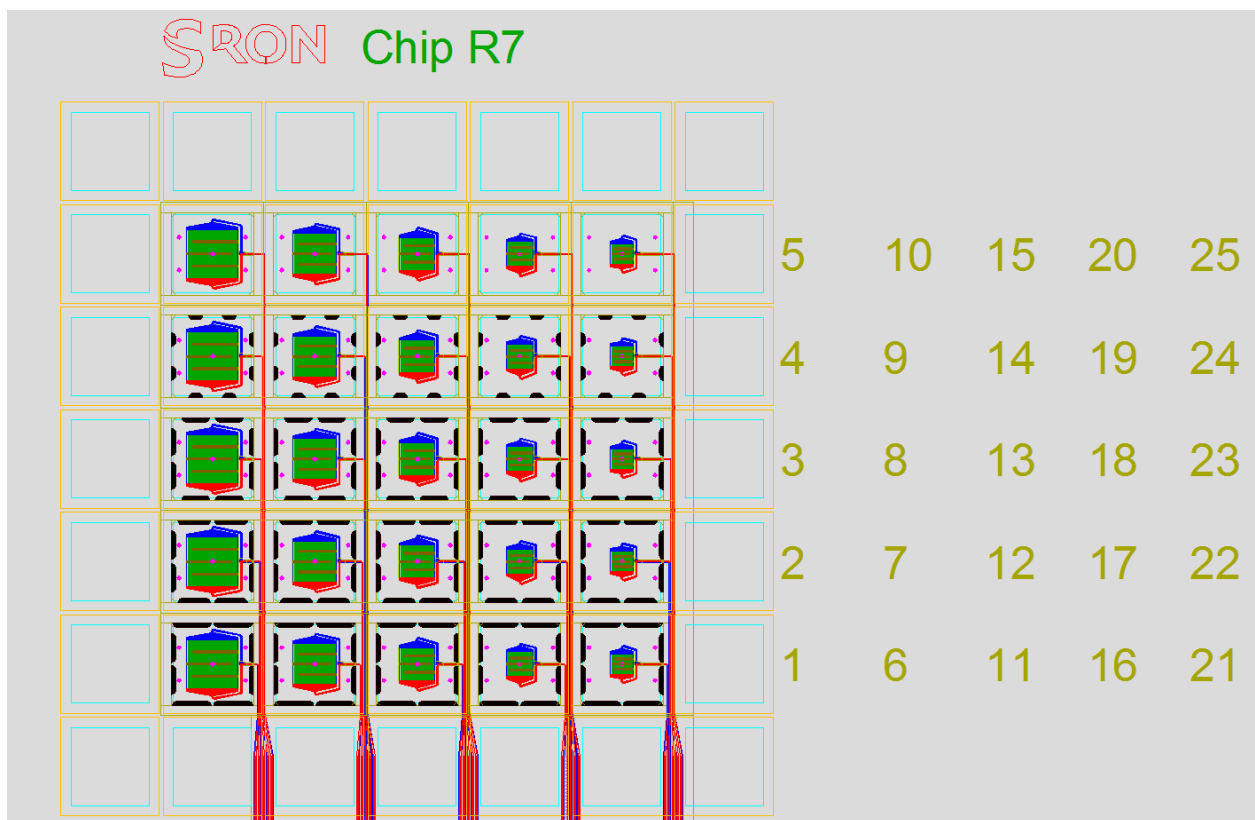


Fig. 4. Pixel array with variable TES area and variable slot size

SRON	TES Detector Development for Athena / X-IFU	
CTP 2015 – WP4 Optimization of a European Transition Edge Sensor Array	TECHNICAL NOTE 2.6	Doc. no.: SRON-XIFU-TN-2015-063 Issue : 1.0 Date : 15-03-2018 Page : 11 of 13

2.4 Chips R9-R10:

These two (identical) chips can be used for further study to the optimum pixel design with respect to wiring connection and TES aspect ratio. The design is complementary to the mask set used for WP 4 so far, since here the Si support structure is representative for the future designs.

Each pixel variation is present in five copies (columns). The variations are:

Set 1					
	1	2	3	4	5
TES:	100x100	140x70	140x50	100x100	100x100
# stripes:	3	5	5	3	3
Stripe length:	80%	80%	80%	80%	80%
Stripe width:	5 μ m				
Wiring loop:	Small	Small	Small	Large	Small
Abs. coupling:	Dot 10 μ m				
Looped wire:	no	no	No	No	Yes

With the TES aspect ratio we change the total resistance of the pixel. This will change the noise properties, but when lowering the Ti/Au square resistance we can retain the matching to the readout circuit.

With nr. 4 we can look to the effect of a larger wiring loop on the AC losses.

With nr. 5 there is a loop of superconducting material around the TES, which alters the sensitivity to magnetic field variations.

The TESes in each row are identical to study the uniformity of the performance with the exact same design.



Fig. 5. Pixel array with variable pixel design set nr. 1.

SRON	TES Detector Development for Athena / X-IFU	
CTP 2015 – WP4 Optimization of a European Transition Edge Sensor Array	TECHNICAL NOTE 2.6	Doc. no.: SRON-XIFU-TN-2015-063 Issue : 1.0 Date : 15-03-2018 Page : 12 of 12

2.5 Chips R11-R12:

These two (identical) chips can be used for further study to the optimum pixel design with respect to the absorber coupling. The T-shaped coupling as used by GSFC is considered too.

Set 2					
	1	2	3	4	5
TES:	100x100	100x100	100x100	100x100	100x100
# stripes:	3	3	0	3	3
Stripe length:	80%	80%	0	80%	80%
Stripe width:	5 μ m	5 μ m	0	5 μ m	5 μ m
Wiring loop:	Small	Small	Small	small	Small
Abs. coupling:	Dot 10 μ m	1 on side	2 on side	2 on edge	T-shape
Looped wire:	no	no	No	No	no

The TESes in each row are identical to study the uniformity of the performance with the exact same design.

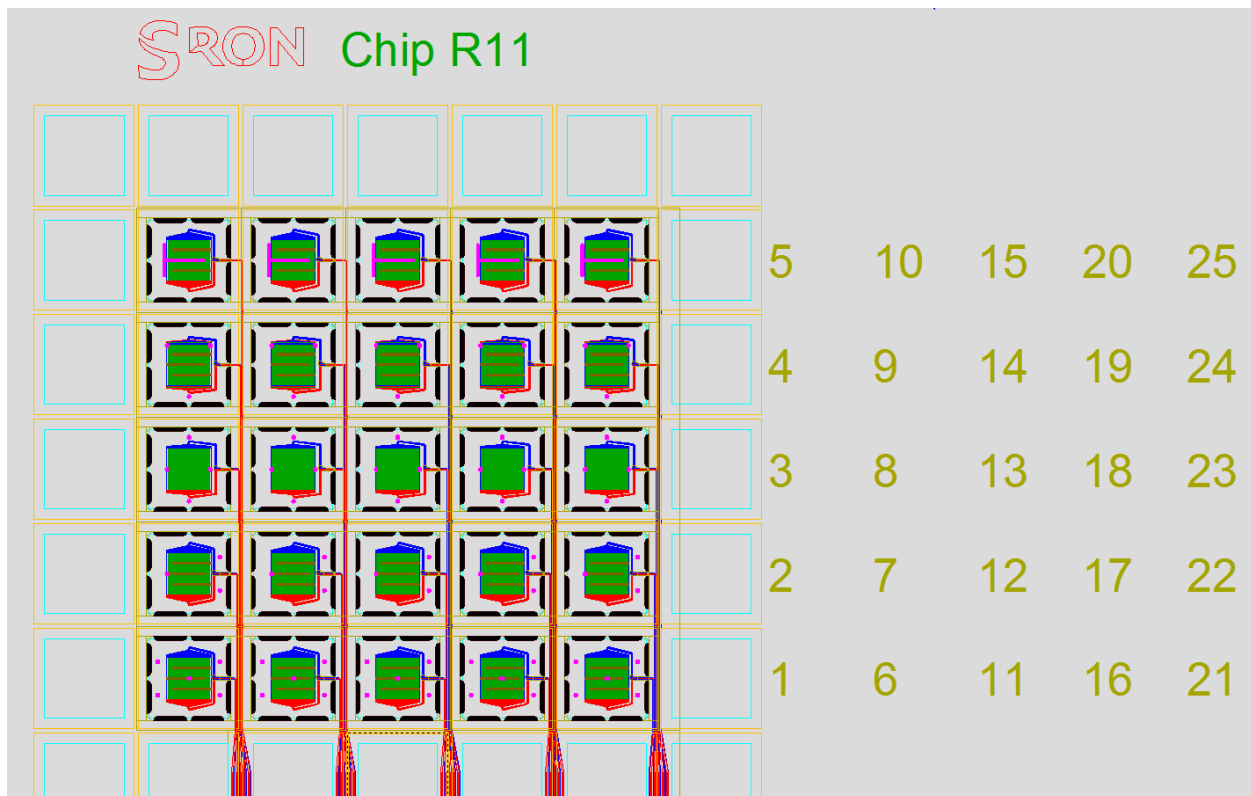


Fig. 6. Pixel array with variable pixel design set nr. 2.